Resource

Cell

Tridimensional Visualization and Analysis of Early Human Development

Graphical Abstract

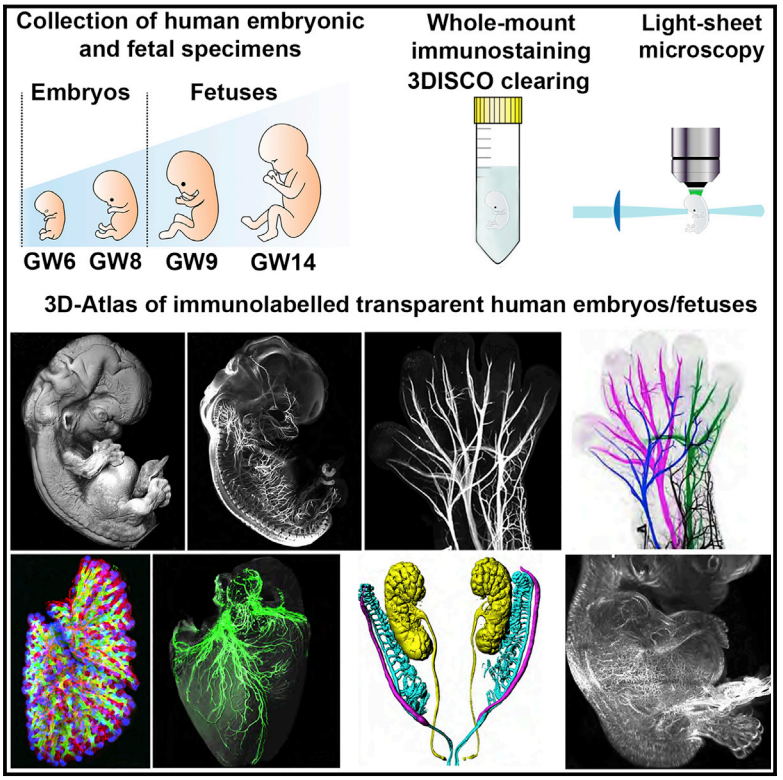

Highlights

- We used 3DISCO/iDISCO+ clearing methods to start building a 3D human cell atlas
- A collection of high-resolution images of whole human embryos and fetal organs
- An interactive online resource and 3D digital database of human development
- Unknown features of human development revealed in cleared and immunostained embryos

Authors

Morgane Belle, David Godefroy, Gérard Couly, Samuel A. Malone, Francis Collier, Paolo Giacobini, Alain Chédotal

Correspondence

alain.chedotal@inserm.fr

In Brief

An initial look at dynamic processes during early human development through 3D cellular imaging.

Belle et al., 2017, Cell *169*, 161–173
March 23, 2017
http://dx.doi.org/10.1016/j.cell.2017.03.008

CellPress

Resource

Cell

Tridimensional Visualization and Analysis of Early Human Development

Morgane Belle,[1] David Godefroy,[1] Gérard Couly,[1] Samuel A. Malone,[2,3] Francis Collier,[4,5] Paolo Giacobini,[2,3,4] and Alain Chédotal[1,6,*]

[1]Sorbonne Universités, UPMC Univ Paris 06, INSERM, CNRS, Institut de la Vision, 17 Rue Moreau, 75012 Paris, France
[2]UMR-S 1172, JPArc – Centre de Recherche Jean-Pierre AUBERT Neurosciences et Cancer, University of Lille, Lille 59000, France
[3]INSERM, UMR-S 1172, Laboratory of Development and Plasticity of the Neuroendocrine Brain, Lille 59000, France
[4]FHU 1,000 Days for Health, School of Medicine, University of Lille, Lille 5900, France
[5]Gynaecology Service, Hospital Jeanne de Flandres, CHU Lille, Lille 59000, France
[6]Lead Contact
*Correspondence: alain.chedotal@inserm.fr
http://dx.doi.org/10.1016/j.cell.2017.03.008

SUMMARY

Generating a precise cellular and molecular cartography of the human embryo is essential to our understanding of the mechanisms of organogenesis in normal and pathological conditions. Here, we have combined whole-mount immunostaining, 3DISCO clearing, and light-sheet imaging to start building a 3D cellular map of the human development during the first trimester of gestation. We provide high-resolution 3D images of the developing peripheral nervous, muscular, vascular, cardiopulmonary, and urogenital systems. We found that the adult-like pattern of skin innervation is established before the end of the first trimester, showing important intra- and inter-individual variations in nerve branches. We also present evidence for a differential vascularization of the male and female genital tracts concomitant with sex determination. This work paves the way for a cellular and molecular reference atlas of human cells, which will be of paramount importance to understanding human development in health and disease.

INTRODUCTION

For centuries, the intricacies of human development have remained an enigma and its study unexplored due to sociocultural, religious, and moral reasons (Morgan, 2009). In the second half of the twentieth century, a growing interest in experimental embryology and technological developments (King and King, 1986) led to the first scientific descriptions of human embryo development (His, 1881; Keibel and Elze, 1908). In the middle of the 20th century, Franklin Mall and colleagues at the Carnegie Institute collected, sectioned, and stained thousands of human embryos and fetuses (Morgan, 2009). Wax reconstructions and 3D embryo models were generated (Norman, 1923) to define stages of human embryogenesis, still in use today (Keibel and Mall, 1910; O'Rahilly and Müller, 1987). Similar collections of human embryos were initiated in other countries (Blechschmidt, 1977; Fujimoto, 2001). These data still appear in all modern textbooks and atlases of embryogenesis and developmental biology. More recently, histological sections were digitized and reconstructed in 3D (de Bakker et al., 2016). Immunohistochemical studies have also been performed but lack the 3D information, which is essential to understanding organogenesis. Ex vivo 3D images of paraformaldehyde (PFA)-fixed human embryos were recently obtained by using magnetic resonance imaging or phase-contrast X-ray radiographic computed tomography; however, the resolution is still far from being at the cellular level (Kanahashi et al., 2016; Yamada et al., 2010).

Whole mouse brains and embryos rendered transparent with various procedures can be imaged with excellent cell resolution (Richardson and Lichtman, 2015). Solvent-based clearing methods such as 3DISCO (Three-dimensional imaging of solvent cleared organs) (Ertürk et al., 2011) and its derivatives iDISCO (Renier et al., 2014), iDiSCO+ (Renier et al., 2016), and uDISCO (Pan et al., 2016) are fully compatible with whole-mount immunofluorescence (Belle et al., 2014; Renier et al., 2014). The rise of light sheet fluorescence microscopy (LSFM) has led to the development of imaging setups compatible with large field objectives and thick (>1 cm) specimens (Dodt et al., 2007). We set out to develop a protocol that combines antibody labeling and tissue clearing for better analyses in human embryology.

Here, we have performed whole-mount immunostaining on 36 human embryos and fetuses ranging from 6 to 14 weeks of gestation with over 70 antibodies, most of which had never been used in humans (see STAR Methods and Table S1). We have generated 3D images of human embryos at an unprecedented cellular resolution. This work offers a unique opportunity to start building a molecular and cellular atlas for the study of human development. The possible applications of this new method in the field of embryology are countless. They open new avenues for the study of molecular mechanisms regulating the development of human embryos in physiological and pathological conditions.

RESULTS AND DISCUSSION

Development of the Human Peripheral Nervous System

We used a protocol for whole-mount immunostaining and 3DISCO clearing to analyze the development of human embryos

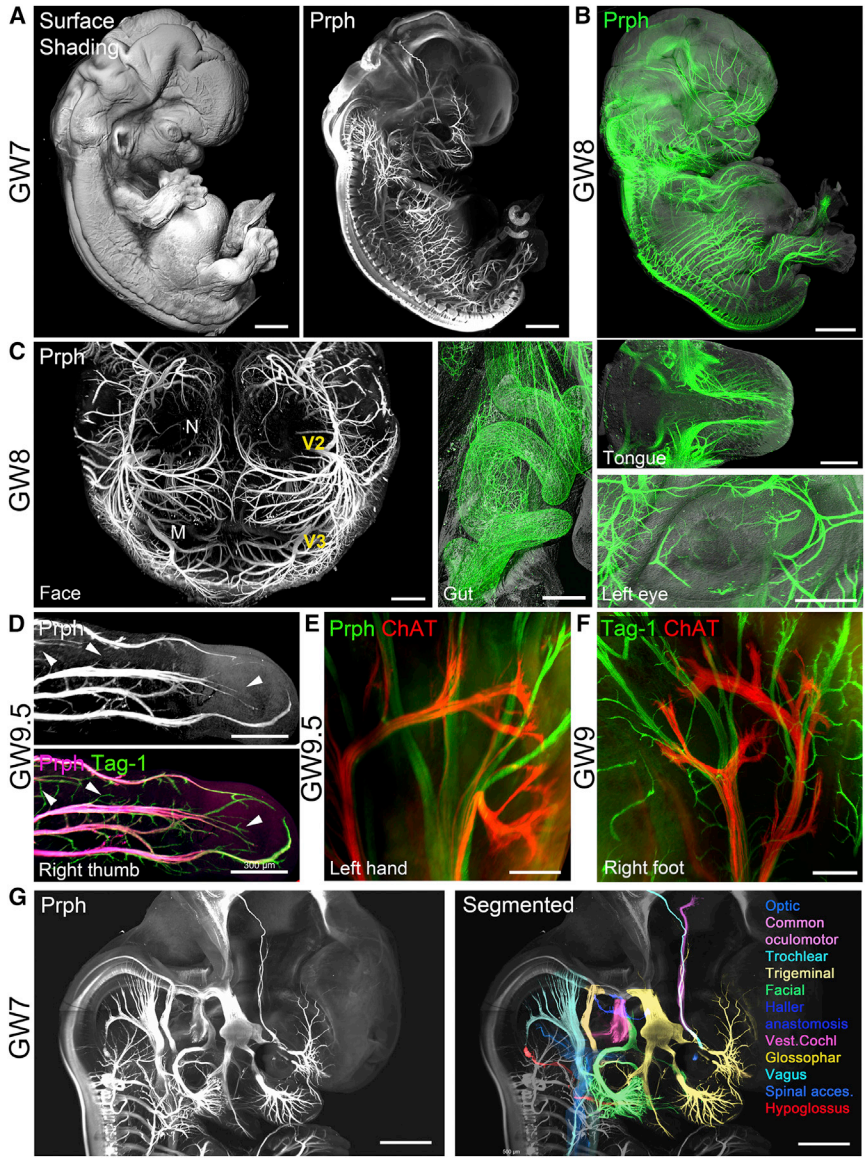

Figure 1. 3D Analysis of Peripheral Nervous System Development in Human Embryos

All panels are LSFM images of solvent-cleared embryos and fetuses.

(A) Surface shading image (left) and Prph labeling of peripheral nerves (right) at GW7.

(B) Overlay of the surface shading image (gray) and Prph labeling (green) at GW8.

(C) High-magnification images of Prph+ innervation at GW8. The middle and right panels are overlays of the surface contrast image (gray) and Prph labeling (green).

(D) GW9.5 thumb labeled for Prph and Tag-1. The two markers co-localize but the thinnest branches (arrowheads) are better labeled with Tag-1.

(E) Dorsal view of a GW9.5 hand double labeled for ChAT (motor axons) and Prph (sensory axons), showing the lack of co-localization.

(F) Dorsal view of a GW9 foot labeled for ChAT and Tag-1. The two markers are not co-expressed.

(G) Right view of the head and cranial nerves at GW7 (Prph staining). On the right panel, cranial nerves are segmented and highlighted with specific pseudo-colors.

Abbreviations: N, nostrils; M, mouth; V2 (maxillary) and V3 (mandibular), second and third branches of the trigeminal nerve.

Scale bars, 1,000 μm in (A) and (G), 2,000 μm in (B), 500 μm in (C), 300 μm in (D), 200 μm in (E), and 150 μm in (F).

See also Figure S1.

(first 8 weeks of gestation) and fetuses (from 8.5 to 14 weeks, see STAR Methods). We first studied the development of the peripheral nervous system (PNS) using antibodies against the neuron-specific intermediate filament protein peripherin (Prph), which in rodents is expressed by sensory and autonomic axons (Parysek et al., 1988). In human fetuses, Prph labels auditory and vomeronasal nerves (Casoni et al., 2016; Locher et al., 2013).

We first used embryos at gestation week 6 (GW6) (or, Carnegie stage CS17, n = 1; see STAR Methods for stage determination), GW7 (CS19, n = 2), GW7.5 (CS21, n = 1), and GW8 (CS23, n = 3). As previously reported for mice (Belle et al., 2014; Renier et al., 2014), tissue-shrinkage was observed (20%–40% of its original size) and remained homogeneous throughout the embryo. This shrinkage can be avoided using iDISCO+ (Renier et al., 2016), however, the cleared embryos produced by this method are more fragile and their fluorescence less stable than with 3DISCO. In addition, the methanol treatment needed for iDISCO+ is not compatible with some antibodies. Last, the size reduction after 3DISCO allowed whole embryos to be imaged via LSFM and Prph+ peripheral nerves to be visualized from the brainstem and spinal cord to their distal extremities (Figures 1A–1C and S1A and S1B and Movie S1).

We next tested specific markers of sensory and motor axons, focusing primarily on the innervation of the developing feet and hands from GW6–GW12. Motor and sensory axons were respectively labeled with antibodies against choline acetyl transferase (ChAT; n = 14 cases) and transient adhesion glycoprotein-1 (Tag-1/Contactin 2; n = 22 cases) (Karagogeos et al., 1997). Double staining for Prph and Tag-1 (n = 14) confirmed that both markers overlapped in peripheral nerves, although from GW9, the thinnest axonal branches were better seen with Tag-1 (Figure 1D). In contrast, there was no overlap between ChAT+ and Prph+ (Figure 1E; n = 6) or ChAT+ and Tag-1+ (Figures 1F and S1C; n = 7) immunoreactive axons. Motor nerve roots were not immunoreactive for Prph (data not shown), suggesting that in humans, Prph is differentially expressed between spinal cord and cranial motor axons.

3D virtual dissection of organ innervation with Imaris segmentation plugins was performed to trace, artificially color, and reconstruct individual nerve fascicles (STAR Methods). This

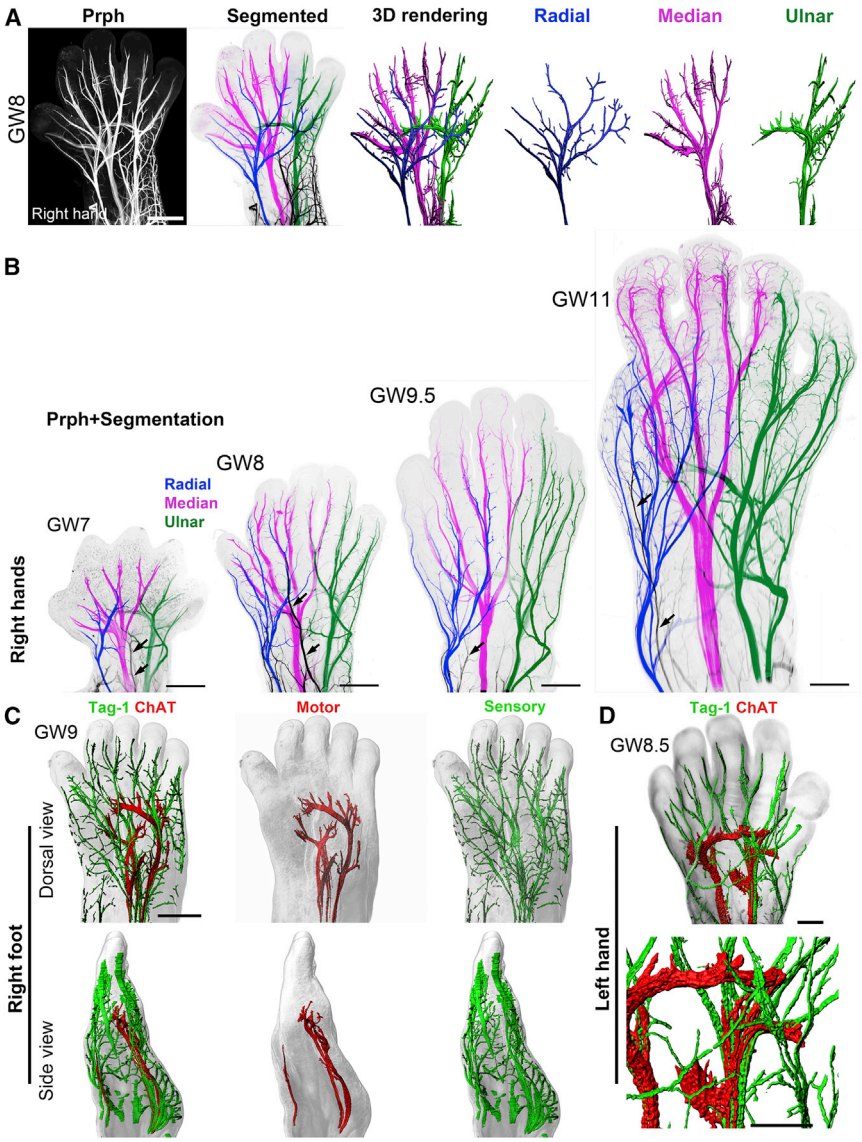

Figure 2. 3D Analysis of the Innervation of the Developing Human Hand and Foot

All panels are LSFM images of solvent-cleared embryos and fetuses.

(A) Images (dorsal view) illustrating the segmentation process of individual sensory nerves in a GW8 hand labeled for Prph. Raw LSFM images (left) and individual segmentation and 3D rendering of the radial (blue), median (magenta), and ulnar (green) nerves (right panels) are shown.

(B) Time series illustrating the developing innervation of the right hand from GW7-GW11 at a similar scale. The musculocutaneous nerve (arrows) transiently extends into the hand.

(C and D) Segmentation of the sensory (Tag-1, green) and motor (ChAT, red) nerves in a GW9 foot (C) and GW8.5 hand (D).

(C) Dorsal views (upper panels) and right side views (lower panels).

(D) Trajectory (dorsal view) of individual motor and sensory axons (lower panel).

Scale bars, 700 μm in (A), 400 μm in (B), 500 μm in (C), 200 μm in (D).

See also Figure S2.

method was applied to GW7 (CS19; n = 2) and GW8 (CS23; n = 1; Figure 1G) cranial nerves (Figures 1G and S1A and Movie S1). Fetuses older than GW8, too large for our LSFM microscope, were dissected prior to processing in order to image limbs and other large organs.

Segmentation-based tracing was used to reconstruct the sensory innervation of the hand from GW6 to GW11.5. The human hand contains the ulnar (or cubital), median, and radial nerves, which innervate different hand areas in a pattern highly conserved between individuals (Unver Dogan et al., 2010).

Sensory nerves and their branches in the hands of 14 embryos and fetuses were reconstructed in 3D using Prph (GW7–GW11, n = 11) or Tag-1 (GW6–GW9.5, n = 3) immunostaining (Figures 2A and 2B and S1D) and used to create a developmental time-lapse of sensory innervation in the human hand (Figure 2B and Movie S2). Furthermore, we reconstructed the motor (ChAT+) and sensory (Tag-1+) innervation of two GW8.5 and GW9 fetuses (Figures 2C and 2D and S1C and Movie S2) to determine where and how the two types of nerves diverge.

We next compared the nerve branching patterns in 11 hands and found, in all individuals analyzed, striking heterogeneity between the left and right hands. At all ages, the median nerve was the most similar (Figure S2A and data not shown), whereas noticeable differences in the number and length of branches existed between the left and right ulnar or radial nerves (Figures S2A and S2B and Movie S2). The low number of cases analyzed did not allow for the detection of any correlation with hand laterality. Interestingly, unlike in adults, the musculocutaneous nerve extended into the hand, at least until GW11 (Figure 2B).

The adult cutaneous innervation is topographically organized with each of the three nerves innervating non-overlapping skin territories. To determine how this map is established, we pseudo-colored the domains overlying Tag-1+ axons in hands at GW6, GW8.5, and GW11.5 (Figure S2C and Movie S2). At GW8.5, most of the hand surface was already covered with nerves whose topography appeared mature by GW11.5. The middle and index fingers are particularly interesting given that their dorsal surfaces are shared by several nerves. The median nerve, which normally only arborizes ventrally, projects to the dorsal side of these fingers. At GW6, the median nerve had not yet reached the tip of the index on the palmar (ventral) side but started to branch dorsally, ahead of the radial nerve, between future phalanges (Figure S2D). By GW8, the median nerve reached the tip of the index finger ventrally and started to cover

the dorsal and distal part, whereas the radial nerve only innervated the caudal part of the dorsal side of the index finger. This pattern was unchanged at later ages (Figure S2D).

Our protocol allows 3D visualization of the development of the peripheral innervation of early human fetal stages (first trimester of life) at a high level of precision and detail and has revealed several unknown features of the development of limb innervation. First, an adult-like pattern of the domains of the skin covered by each nerve is already established during the late embryonic-early fetal period. However, within each domain, the pattern of nerve branching can be highly divergent not only between individuals but also within the same individual. This is particularly striking at the level of the hands, where the arborization of the ulnar and radial nerves significantly differ between the right and left hands. This suggests that the development of the PNS innervation is, at least to some extent, stochastic and not profoundly influenced by specific guidance cues distributed in the developing limbs and extremities (Hassan and Hiesinger, 2015). Moreover, in digits that are shared by multiple nerves there is no significant overlap of the branches originating from the different nerves. Our data infer that median nerves grow faster and start invading the dorsal part of some digits prior to the other nerves and that this may prevent them from entering these territories. Finally, significant remodeling of the sensory innervation occurs. The length of human embryogenesis, as compared to that of rodents, will facilitate the analysis of tissue remodeling during development.

Next, we further validated our method by testing a large palette of antibodies against proteins expressed by many cell types in developing mouse and human embryos (STAR Methods).

3D Analysis of Human Muscle Development via LSFM

The current knowledge of skeletal and head muscle development in humans is based on histological studies conducted during the first half of the twentieth century (Gasser, 1967; Gilbert, 1957) and immunostaining with a few muscle cell markers (Abe et al., 2010; De la Cuadra-Blanco et al., 2013). The distribution of muscle cell progenitors in the embryo, however, has never been reported. The transcription factor (TF) Pax7, is a muscle stem cell marker and key initiator of myogenesis in jawed vertebrates (Bryson-Richardson and Currie, 2008). We observed Pax7 immunoreactive nuclei homogenously distributed within each developing muscle of GW9.5 and GW10.5 arms and legs (Figures 3A and 3B and Movie S3; n = 1). As expected, all developing Pax7+ muscles were contacted by ChAT+ motor branches (Figure 3B). GW9 leg and arm (n = 1) were also triple-immunostained for ChAT, Tag-1, and myogenin (Myog), a myogenic TF expressed by differentiating myoblasts (Bryson-Richardson and Currie, 2008) (Figure 3C and Movie S3). This immunostaining shows that clusters of Myog expressing cells are found at the extremities of each motor nerve branch.

Doublecortin (Dcx) is an X-linked gene that encodes a microtubule-associated protein (Gleeson et al., 1998; des Portes et al., 1998). Mutations in *DCX* impede neuronal migration and cause lissencephaly. Dcx may also influence the development of the neuromuscular junction in humans (Bourgeois et al., 2015). Dcx immunostaining on limbs at GW8 (n = 1), GW9.5 (n = 1), GW10 (n = 1), GW10.5 (n = 1), and GW13.5 (n = 1) showed that developing muscles express Dcx (Figure 3D and data not shown). Sensory nerves were also immunoreactive for Dcx (Figure 3D). Myosin heavy chain (MHC) was previously detected in skeletal, heart, and craniofacial muscles from human fetuses (Abe et al., 2010). Here, we studied the distribution of MHC+ muscles throughout the body at GW8–GW14 (Figure 3E and Movie S3; n = 9 cases). All muscles in the upper half of a GW8 embryo (n = 1) were labeled and identified with an unprecedented resolution (Figure 3E and Movie S3). Whole-mount MHC muscle staining was also performed on GW11 and GW14 arms and legs (Figures S3B and S3C). Developing muscles and motor innervation could be simultaneously visualized following MHC/ChAT double immunostaining (Figure 3F and not shown), and importantly, the muscles within each hand and foot of a GW9.5 fetus could be segmented (Figures 3F and S3A and S3D and Movie S3). Moreover, the shape of the developing bones, which appear as black areas on optical sections, could also be extracted and visualized in 3D (Figure S3D).

3D Analysis of the Vasculature in Human Embryos

Existing data based on the filling of large arteries and veins (Mall, 1905), 3D reconstructions of histological sections (de Bakker et al., 2016), and vascular corrosion casting (Zawiliński et al., 2001) provide an incomplete view of the early development of human vasculature. In chicks and mice, blood vessels arise from endothelial cell progenitors (angioblasts), which aggregate to form a dense vascular meshwork covering the embryo, a process known as vasculogenesis (Chung and Ferrara, 2011). Functional continuity occurs later through the remodeling of this initial endothelial network. As the embryo grows, new vessels sprout from existing ones, in a process called angiogenesis. Here, we first performed whole-mount labeling with antibodies against plasmalemma vesicle-associated protein (Plvap; also known as PV-1 or PAL-E), a transmembrane glycoprotein expressed by fenestrated microvascular endothelial cells (Elima et al., 2005). Whole embryos at GW8 (n = 2) or various organs from GW9.5–GW14 fetuses (n = 8) were labeled and imaged with LSFM. At GW8, an extremely dense Plvap+ vascular network of endothelial cells extended throughout the body (Figure 4A and Movie S4), except in developing bones and corneas (Figure 4B and Movie S4). This supports the existence of a phase of vasculogenesis preceding angiogenesis in human embryos. Among other endothelial cell markers tested, collagen IV also labels capillaries, but less efficiently than Plvap (Figure 4C). The 3D organization of developing arteries on GW9–GW14 organs (n = 6 fetuses) were assessed with immunostaining for smooth-muscle-specific α-actin (SMA) (Figure 4D and Movie S4).

Mammalian lymphatic vasculature development is documented for several species (Yang and Oliver, 2014), but not much is known about human lymphangiogenesis (Sabin, 1909). The lymphatic system is crucial for immune response and understanding its development might allow us to gain some insights into some human diseases. To start investigating lymphangiogenesis in human fetuses, we next labeled the gastrointestinal tract of a GW14 fetus with antibodies against the glycoprotein podoplanin, a lymphatic cell marker (Breiteneder-Geleff et al., 1999; Schuster et al., 2015), and found many isolated podoplanin+ cells covering the gut and stomach (Figure 4E). Lymphatic

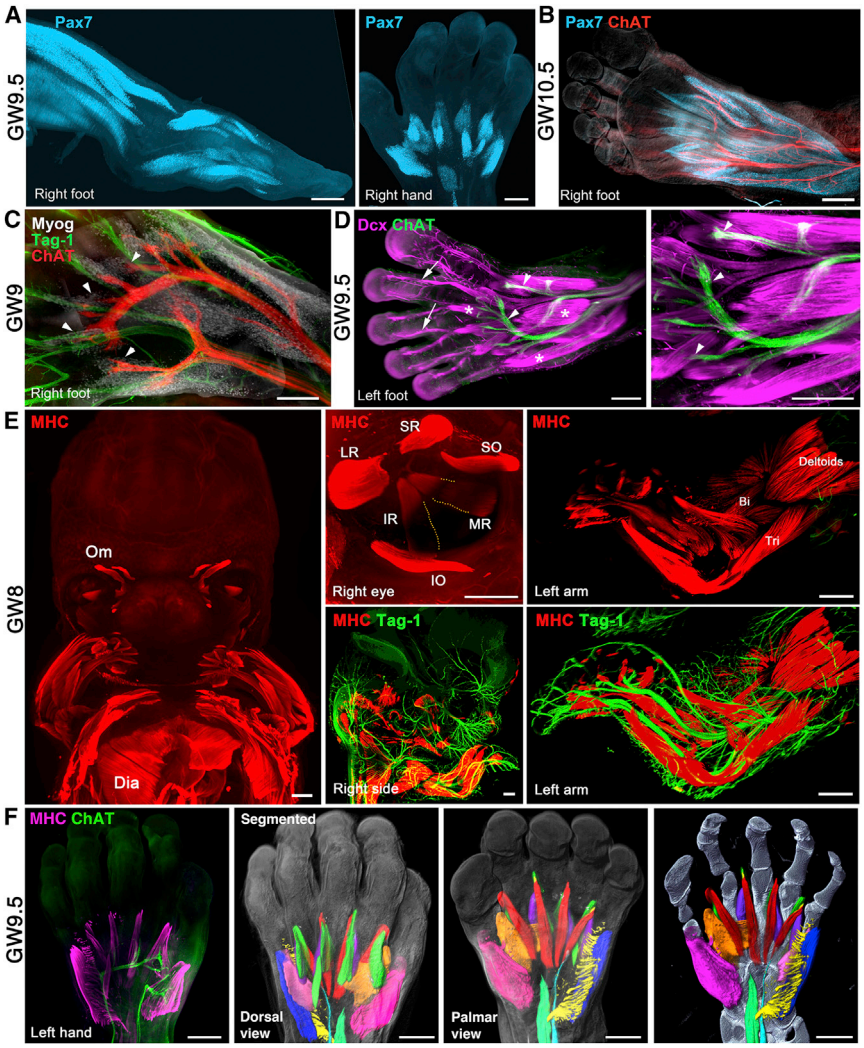

Figure 3. 3D Analysis of Muscle Development in Human Embryos

All panels are LSFM images of solvent-cleared embryos and fetuses.

(A) Lateral view of the right foot (left panel) and dorsal view of the right hand (right panel) of a GW9.5 fetus labeled for Pax7.

(B) Plantar view of a GW10.5 foot labeled for Pax7 (blue) and ChAT (Red).

(C) Dorsal view of a GW9 foot labeled for Myog, ChAT, and Tag-1. Myog+ nuclei cluster at the tip of ChAT+ motor branches (arrowheads).

(D) Dorsal view of a GW9.5 foot double-labeled for Doublecortin (Dcx) and ChAT. Dcx is found in muscles (asterisks) and sensory nerves (arrows) but not in ChAT+ motor axons (arrowheads).

(E) Images from a GW8 embryo immunolabeled for MHC and Tag-1. Front view (left). High-magnification view of the oculomotor muscles (upper middle panel). The dotted lines mark the borders of the muscles where the light sheet is weakened by the pigmented epithelium. Lateral view (lower middle panel) of muscles and sensory nerves. The right panel shows muscles and sensory nerves in the left arm.

(F) GW9.5 hand labeled for MHC and ChAT showing muscles and motor innervation. Muscles were individually segmented and pseudo colored (see Figure S3A for muscle names), and developing bone contours are visualized (see methods).

Abbreviations: SR, superior rectus; LR, lateral rectus; IR, inferior rectus; MR, medial rectus; IO, inferior oblique; SO, superior oblique; Om, oculomotor muscles; Dia, diaphragm; Bi, biceps; Tri, triceps.

Scale bars, 300 μm in (A) and (D), 500 μm in (B) and (E), 200 μm in (C), 400 μm in (F).

See also Figure S3.

cells could also be seen by using Prox-1 staining (data not shown). The lack of podoplanin+ capillaries at this age suggests that, as in other mammals, the human lymphatic system might mature later than the vascular system.

Lung Development in Human Embryos

In human embryos, the lung primordia and the trachea emerge from the foregut endoderm around CS11/GW4 (O'Rahilly and Müller, 1987), and airway branching proceeds from GW6 to GW16 during the pseudoglandular stage (Galambos and deMello, 2007). New bronchial branches, which bud from existing ones, further divide and lead to an expansion of the tree. Only a few immunohistological studies of human embryo lungs have been conducted (Sparrow et al., 1999). Here, we performed whole-mount immunostaining with 11 antibodies on lungs from 8 embryos and fetuses at GW8–GW14.

In the mouse, the sex determining region Y (SRY)-box 9 (Sox9) TF is expressed in alveolar epithelial cell progenitors at the distal part of each lung branch (Rockich et al., 2013), whereas Sox2 is restricted to the proximal part (Maeda et al., 2007). We observed a similar result in human lungs where all terminal bronchial buds were Sox9+ (Figures 5A–5D, 5H, and S4A and Movie S5), whereas Sox2 was expressed in a complementary pattern (Figures S4A and S4D). Strikingly, double staining for Sox9 and Dcx, which was not yet reported to be present in the lung epithelium, showed that Dcx was also expressed in the proximal epithelial portion of each airway (Figures 5A and 5B). We also visualized in 3D the vasculature of the lung with Plvap (Figures 5A–5C and S4B). The small capillary plexuses in the lung mesenchyme wrapping around terminal buds at GW8 are not isolated but form a continuous network with the larger vessels (Figures 5A–5C and S4B), thereby supporting an angiogenesis mode of lung vascularization as observed in mice (Parera et al., 2005).

The complete reconstruction of the mouse airway lineage revealed that the branching pattern is highly stereotyped with new branches budding according to 3 modes: domain branching (daughter branches form in a row) and planar and orthogonal bifurcation budding (Metzger et al., 2008). We performed such a lineage analysis in human whole lungs by using the segmentation

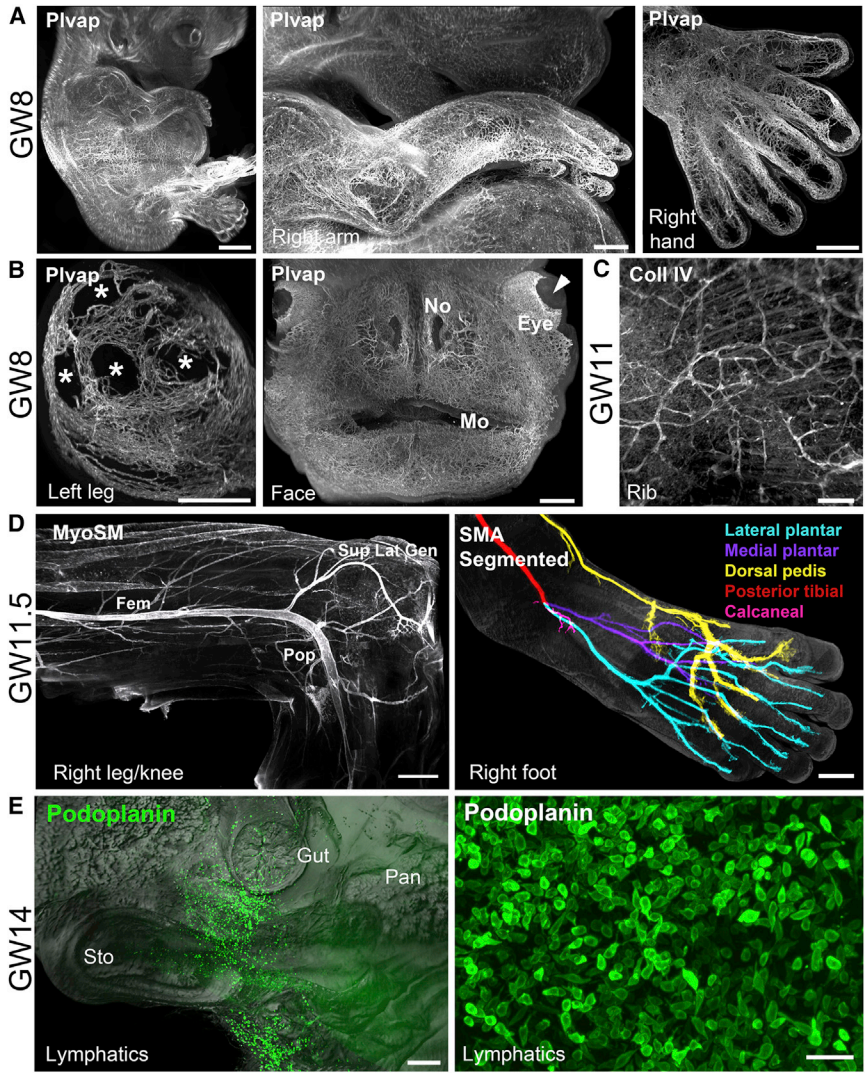

Figure 4. 3D Analysis of the Developing Vascular System in Human Embryo

All panels are LSFM images of solvent-cleared embryos and fetuses.

(A and B) GW8 embryo immunolabeled for Plvap, a marker of endothelial cells. Plvap+ cells form a very dense network throughout the embryo. The right panels in (A) illustrate the right arm and hand.

(B) The left panel is a z projection of 1,400 μm through the left leg. The vascular network penetrates all tissues except the developing bones (asterisks). The right panel is at the level of the face. Note the absence of vessels on the developing cornea (arrowhead).

(C) Vessels labeled with collagen IV at the surface of the ribs in a GW11 fetus.

(D) Arteries in the right leg/knee and foot of a GW11.5 fetus immunolabeled for MyoSM (left) or SMA (right). The right panel shows the result of the segmentation and individual colorization of the main arteries of the foot (dorsal view).

(E) Image at the level of the digestive tract of a GW14 fetus labeled for podoplanin, a marker of lymphatic cells. Podoplanin cells are found above the stomach (Sto) and gut. The right panel shows that podoplanin+ cells have not yet developed into vessels.

Abbreviations: No, nostrils; Mo, mouth; Fem, Femorale arteria; Sup Lat Gen, arteria superiori lateralis genus; Pop, arteria popliteal; Pan, pancreas.

Scale bars, 1,500 μm in the left panel of (A), 500 μm in the right and middle panels (A) and in (B), (D), and the left panel of (E), 200 μm in (C), and 50 μm in the right panel of (E).

of Sox9/Dcx (or Sox9/Sox2) bronchioles (Figures 5D and 5E and Movie S5). We observed three branching modes in humans (Figure 5E), similar to the mouse, but with some evidence of asymmetric bifurcations (Figure 5E). We next performed immunolabeling for smooth muscle markers SMA and myosin smooth muscle (MyoSM). In both cases, smooth muscles surrounding the bronchi and the proximal part of airway epithelial tubules were labeled (Figures 5F and 5G and S4A). The absence of smooth muscles on distal buds was confirmed by using Sox9 immunostaining (Figure 5H). Incidentally, smooth muscle staining also allowed to visualization of lung arteries and arterioles (Figures 5F and 5G and Movie S5).

The lung is primarily innervated by sympathetic and parasympathetic axons traveling through the vagus nerve. Parasympathetic ganglia also contribute to the innervation of the trachea and main bronchi (Aven and Ai, 2013). Due to the complexity of the airway tree, understanding its innervation can only be achieved in 3D. We visualized lung innervation by using immunostaining against Prph, Tag-1, and ßIII-tubulin. Immunoreactive vagus axons extended to the most distal portion of the airway branches (Figures S4C and S4D). Preliminary results indicate that the development of the vasculature of the human heart and its innervation (using immunostaining for Tyrosine hydroxylase) can also be studied with this 3D method (Figures 5I and 5K and S4E and Movie S5).

3D Analysis of Urogenital System Development in Human Embryos

In adult mammals, the urogenital system is comprised of the kidneys, urinary tracts, gonads, and reproductive ducts. Before GW7–GW8, the human gonadal ridges are undifferentiated. Genital ducts appear morphologically similar in both sexes with two paired structures: the Wolffian ducts (WDs), which are derived from the mesonephros, and the Müllerian ducts (MDs), whose differentiation is induced and guided by the WD. A major reorganization of the genital tracts accompanies sex determination (Jacob et al., 2012; Orvis and Behringer, 2007). In males, MDs regress under the influence of an anti-Müllerian hormone produced by the testes. In females, the WDs degenerate and the MDs transform into the female reproductive ducts (Georgas et al., 2015; O'Rahilly, 1983).

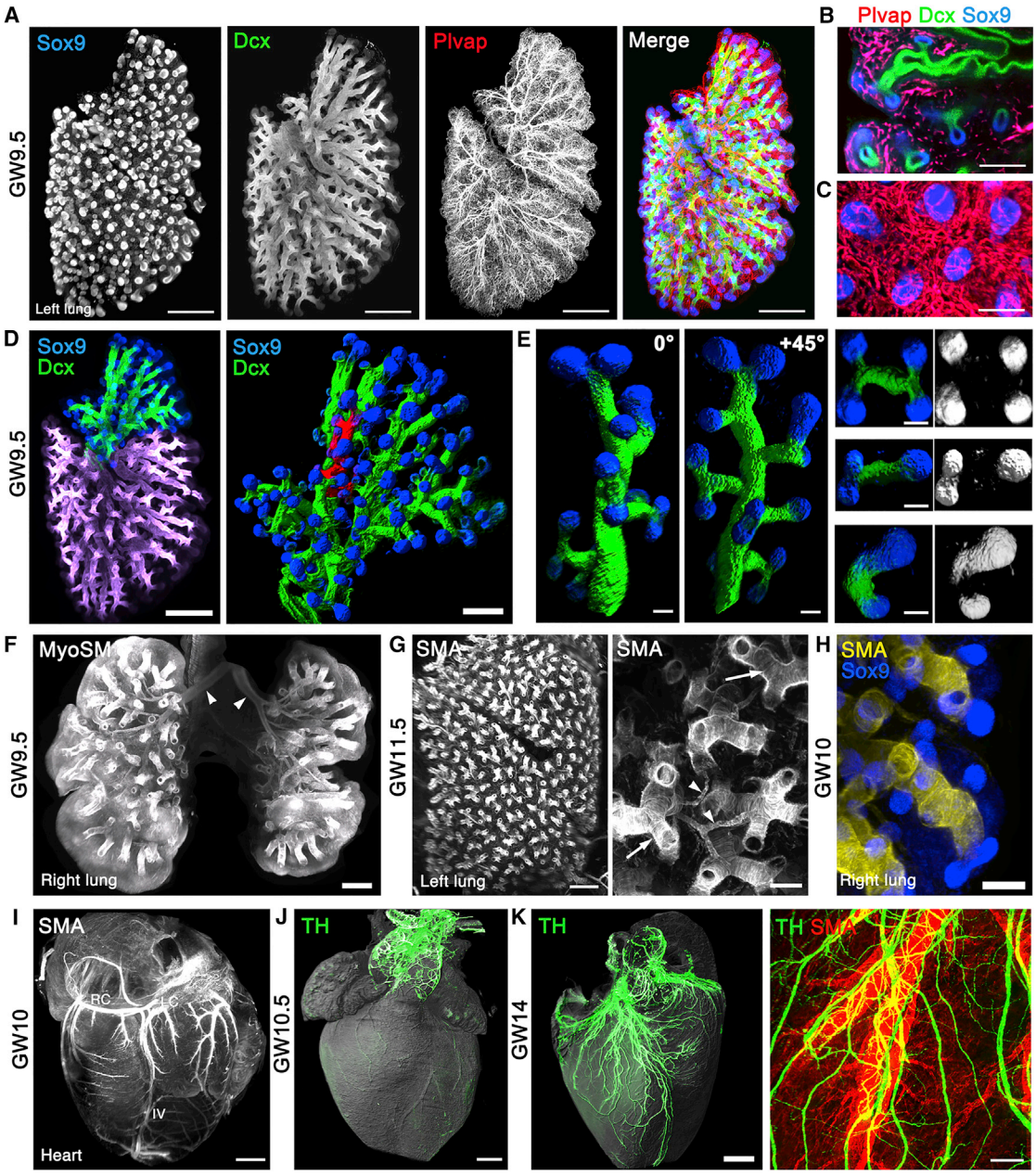

Figure 5. 3D Analysis of the Developing Cardiopulmonary System in Human Embryos

All panels are LSFM images of solvent-cleared fetuses.

(A–E) Left lung from a GW9.5 fetus immunostained for Sox9, Dcx, and Plvap. Sox9 is expressed in the distal bud of the epithelial tubules, whereas Dcx is found in their proximal part. The entire lung vasculature can be labeled with Plvap.

(B) Optical section (250 μm z projection) showing one lung epithelial tubule.

(C) Illustrates the capillary network (red) at the level of Sox9+ terminal buds (blue).

(D and E) 3D Analysis of airway branching. One lung lobe (green and blue) is isolated with Imaris (right panel), and in (D) a single bronchus is isolated (appearing in red).

(E) Higher magnification images of the isolated bronchus viewed under two different angles. The rightmost panels illustrate three types of branching patterns.

(F) GW9.5 lungs stained for myosin smooth muscle (MyoSM). The two main bronchi (arrowheads) and their ramifications are seen.

(G) SMA staining revealing the pattern of airway smooth muscle branching in a GW11.5 left lung. Muscles around arteries (arrowheads) and proximal airways (arrows) are seen.

(H) GW10 lung branches. The terminal buds are labeled with Sox9. SMA+ smooth muscles (yellow) are only found around the proximal portion (Sox9−) of the tubules.

(I–K) LSFM images of the developing heart.

(legend continued on next page)

Knowledge of urogenital system development is primarily based on histological and electron microscopy analysis (Fritsch et al., 2012; Hashimoto, 2003) and has not yet been studied at a cellular and molecular level in humans, unlike in mice (Georgas et al., 2015; Little et al., 2007). We studied the development of the human urogenital system by using antibodies against Pax2 TF. Pax2 mRNA was previously detected in the mesonephros and WD at GW6–GW7 (Tellier et al., 2000). We used embryos and fetuses of either sex, including 11 males (GW8–GW14) and 9 females (GW7–GW14). All major components of the urogenital system were visualized in 3D (Figures 6, 7, and S5 and Movie S6) and individually segmented. In the youngest male embryo (GW8), the caudal tip of the MD was in close contact with the WD but had not yet fully elongated (Figures 6A and 6B), and mesonephric tubules stemming from the WD covered the testis primordium. Kidneys still occupied a ventral position adjacent to the genital ridges (Figure 6A). At GW9.5 (n = 1), the MD further elongated along the WD but did not yet join (Figures 6C and 6D). In GW10 male fetuses (n = 2), the two MD were fused and extended medially between the two WD up to the urogenital sinus. However, in both cases, the MD started to fragment dorsally (Figures 6E and 6F and Figure S5A), and this remnant of the fused MD might give rise to the prostatic utricle. At older ages, such as GW14 (n = 1), the mesonephric nephrons of the WD have regressed while the epididymis ducts and vas deferens have emerged (Figure 6G). As previously reported (Jacob et al., 2012), an apical MD remnant is still present next to the rete testis by GW14 (Figures 6G and 6J and Movie S6). Sox9 is essential to testes differentiation in males, and its mRNA was first detected around CS19–CS21 (GW7–GW7.5) (Hanley et al., 2000). Using whole-mount immunostaining for Sox9 on GW10, GW11, GW13.5, and GW14 fetuses (n = 1 for each), we visualized the 3D organization of the testes cords, containing Sox9+ Sertoli cells (Figure 6H and 6J, Movie S6, and data not shown). We also stained GW10.5–GW13 female fetuses with Pax2 (n = 6) and followed in 3D the reorganization of the urogenital tract (Figures 7 and S5). In our youngest female fetus (GW10.5) the MD have already fused to form the uterovaginal canal (Figure 7A). The WD were still continuous but mesonephric tubules began to regress. At GW11.5, the regression of the mesonephros and WD was more pronounced and the length of the two MD increased (Figure 7B). At GW13, the distal part of the WD had dissolved whereas its cranial part transformed into the Fallopian tubes (Figures 7C and S5B and Movie S6). The vascularization of the developing gonads is thought to play a role in their maturation (Brennan et al., 2002; Coveney et al., 2008). We performed double staining for Pax2 and Plvap to study the interaction between the vasculature and the genital tracts. Interestingly, at GW8 and GW10, the developing testes and WD were embedded in a dense capillary meshwork but the MD was avascular (Figures 7D and 7E). In contrast, in a GW10.5 female fetus, both the MD and the WD were vascularized and a dense vascular network ensheathed the MD by GW13 (Figures 7F and 7G and Movie S6). While we could not study younger female embryos, these results suggest that MD angiogenesis may be sex dependent. This differential vascularization of the developing MD in males and females at GW10 suggest that their regression in males, which starts around this stage, could be linked to or facilitated by the lack of vascularization. By contrast, the WD are vascularized in both sexes. Interestingly, the distal fused part of the Müllerian ducts does not seem to regress and likely gives rise to the prostatic utricle, as previously proposed (Jacob et al., 2012).

Information on the early development of human nephrons is scarce (Ludwig and Landmann, 2005). Staining of GW10–GW13.5 kidneys (n = 5) showed that Pax2 and Sox9 are both expressed in the epithelium of the ureteric tree (Figure S6). Pax2, together with another TF, Six2, was also found in nephron precursors of the cap mesenchyme surrounding the ureteric tips in the nephrogenic zone of the developing kidney (O'Brien et al., 2016). Staining of the endothelial cells with Plvap revealed the presence of developing glomeruli and their morphology (Figure S6D).

Transcription Factors: New Tools to Study Human Embryology

During development, cell differentiation toward specific lineages is controlled by a cascade of transcription factors. We used antibodies against 19 transcription factors to follow the development of multiple organs.

In mouse and human embryos, Sox10 is expressed by oligodendrocytes, neural crest cells, and some of their derivatives (Betters et al., 2010; Bondurand et al., 1998). *SOX10* mutations cause various diseases such as neurocristopathies, melanoma, and peripheral demyelinating neuropathies (Bondurand and Sham, 2013). Here, we performed double immunostaining for Sox10 and Prph on limbs from five fetuses, at GW9–GW12. Sox10+ cells were widely distributed throughout the PNS, at the level of the dorsal root ganglia and all along Prph-labeled nerves and branches (Figure S7A and Movie S7). These Sox10+ cells most likely correspond to Schwann cell precursors, which in the mouse migrate along PNS axons (Espinosa-Medina et al., 2014).

In the developing tongue, taste bud primordia and papillae have been identified at GW9–GW10 by using electron microscopy (Hersch and Ganchrow, 1980). No markers of developing human taste buds are known. In order to visualize tongue papillae, we performed immuno-labeling with antibodies against Prox1 and Sox2, both of which control mouse taste bud differentiation (Nakayama et al., 2015; Okubo et al., 2006). Both Prox1

(I) GW10 heart vasculature stained with anti-SMA antibodies.
(J–K) Evolution of the dopaminergic innervation (TH, tyrosine hydroxylase) of heart between GW10.5 (J) and GW14 (K). The right panel in (K) illustrates the sympathetic innervation (green) on large vessels of the heart (red). See also Figure S4E.
Abbreviations: RC, right coronary artery; LC, left coronary artery, IV, interventricular artery.
Scale bars, 500 μm in (A), (D, left panel), (G, left panel), (I), and (J), 150 μm in (B), (C), (G, right panel), and (K, right panel), 200 μm in (D, right panel), 50 μm in (E), 300 μm in (F), 100 μm in (H), and 1,000 μm in (K, left panel).
See also Figures S4 and S7.

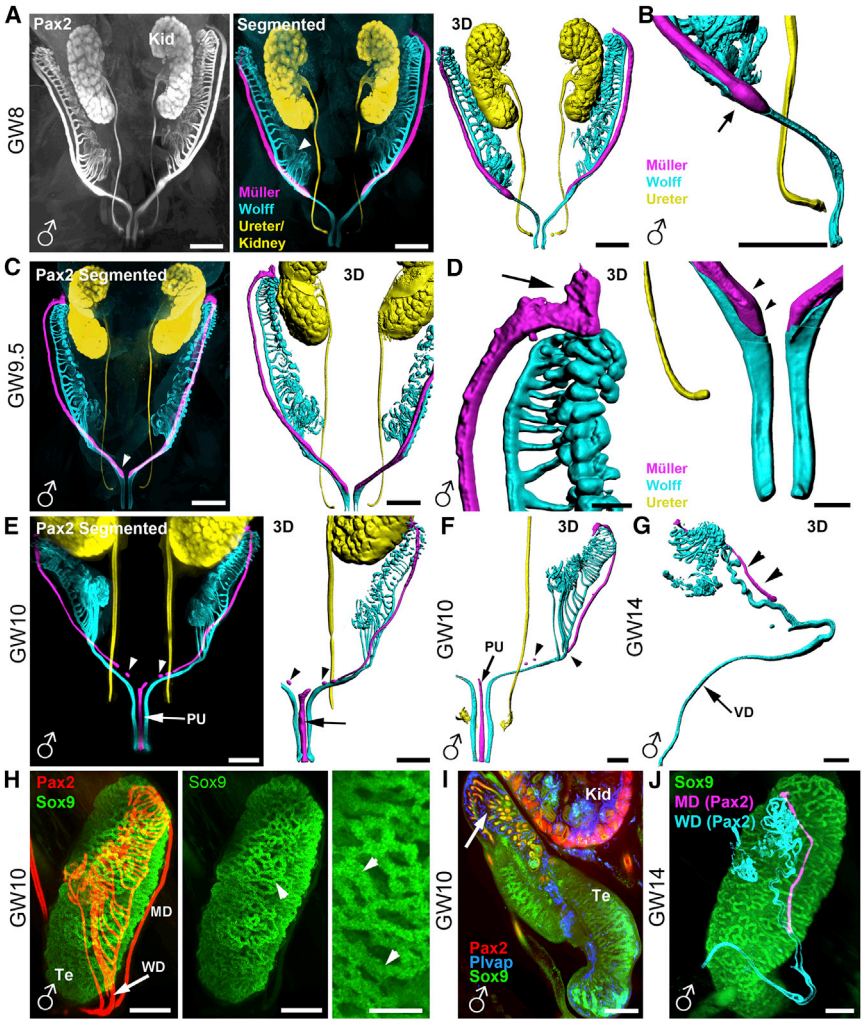

Figure 6. 3D Analysis of the Urogenital System Development in Male Embryos

All panels are LSFM images of solvent-cleared embryos and fetuses.

(A and B) GW8 embryo stained for Pax2. Raw LSFM image (left) and 3D rendering image (right). The middle panel shows the segmentation and pseudocolorization of the kidney and ureters (yellow), Müllerian ducts (magenta, MD), and Wolffian ducts (cyan, WD; the mesonephric tubules are indicated by an arrowhead).

(B) High magnification of the MD/WD junction (arrow).

(C and D) Segmented (left) and 3D (right) images of the GW9.5 urogenital system labeled with Pax2. (D) The apical tip has enlarged (arrow). The distal tips of the MD (arrowheads in C and D) have extended along the WD (compare with A) but have not yet fused.

(E) Segmented (left) and 3D (right) images of the GW10 urogenital system labeled with Pax2. The MD have fused distally (arrow) and began to fragment (arrowheads).

(F) More advanced stage of MD regression and fragmentation (arrowhead) in a second GW10 fetus.

(G) 3D image of the GW14 urogenital system labeled with Pax2. A short fragment of the Müllerian duct persists (arrowhead) and the vas deferens (VD) appears more developed (arrow).

(H) GW10 testis (Te) labeled with Pax2 (red) and Sox9 (green). Sox9+ Sertoli cells are seen in the developing testis cords (arrowheads).

(I) Single optical section (2 μm z projection) through a GW10 fetus testis labeled for Pax2, Sox9, and Plvap (endothelial cells). The arrow indicates the rete testis.

(J) GW14 testis labeled for Sox9 and Pax2 segmented. The Müllerian (magenta) and Wolffian (cyan) ducts (Pax2+) have been segmented and pseudocolored.

Abbreviations: Kid, kidney; MD, Müllerian duct; PU, prostatic utricle; WD, Wolffian duct; ♂, male.

Scale bars, 400 μm in (A), (B), 500 μm in (C) and (E), 100 μm in (D) and (H, right panel), 300 μm in (F), (G), (H, left and middle panels) and (I), and 350 μm in (J). See also Figure S5 and Figure S6.

and Sox2 were detected in lingual papillae (including circumvallate papillae) covering the surface of the tongue (Figure S7B and S7C and Movie S7) in a similar pattern, suggesting that they are co-expressed in taste bud precursors, as observed in mice.

Whole-mount immunostaining for Sox2, which is known to be expressed by many types of cell progenitors (Sarkar and Hochedlinger, 2013), was also performed on other tissues from GW9.5, GW10, and GW12 fetuses. Strikingly, Sox2 expression was detected at the tip of each digit, in a narrow ring of cells lining the edge of the developing nails (Figure S7D and Movie S7). This indicates that Sox2 is a marker of fingernail stem cells in human fetuses, suggesting a role for this TF in nail development. Sox2 was also highly expressed in the ventricular zone of the developing brain (Figure S7E). Finally, we focused on the digestive system, which was collected in embryos and fetuses from GW7 to GW14 (n = 13). Staining with Sox9 clearly revealed the 3D organization of the developing villi of the gut epithelium where stem cells express this TF (Figure S7F and Movie S7) (Bastide et al., 2007). The enteric nervous system (ENS) has recently been the focus of many studies in part because of its frequent involvement in several genetic diseases (Heanue and Pachnis, 2007). ENS neurons are derived from neural crest cells, which colonize the gut around GW4. Double labeling for Phox2b (paired-like homeobox 2b) and Prph revealed the dense network of ENS neurons, which formed interconnected clusters covering the surface of the gut (Figure S7G and Movie S7). Prph staining also revealed the parasympathetic innervation of the digestive system (Figure S7G).

CONCLUSION

Here, we have combined immunolabeling with whole-body and whole-organ 3D imaging to provide a new comprehensive and unbiased method to study the early development of multiple human biological systems.

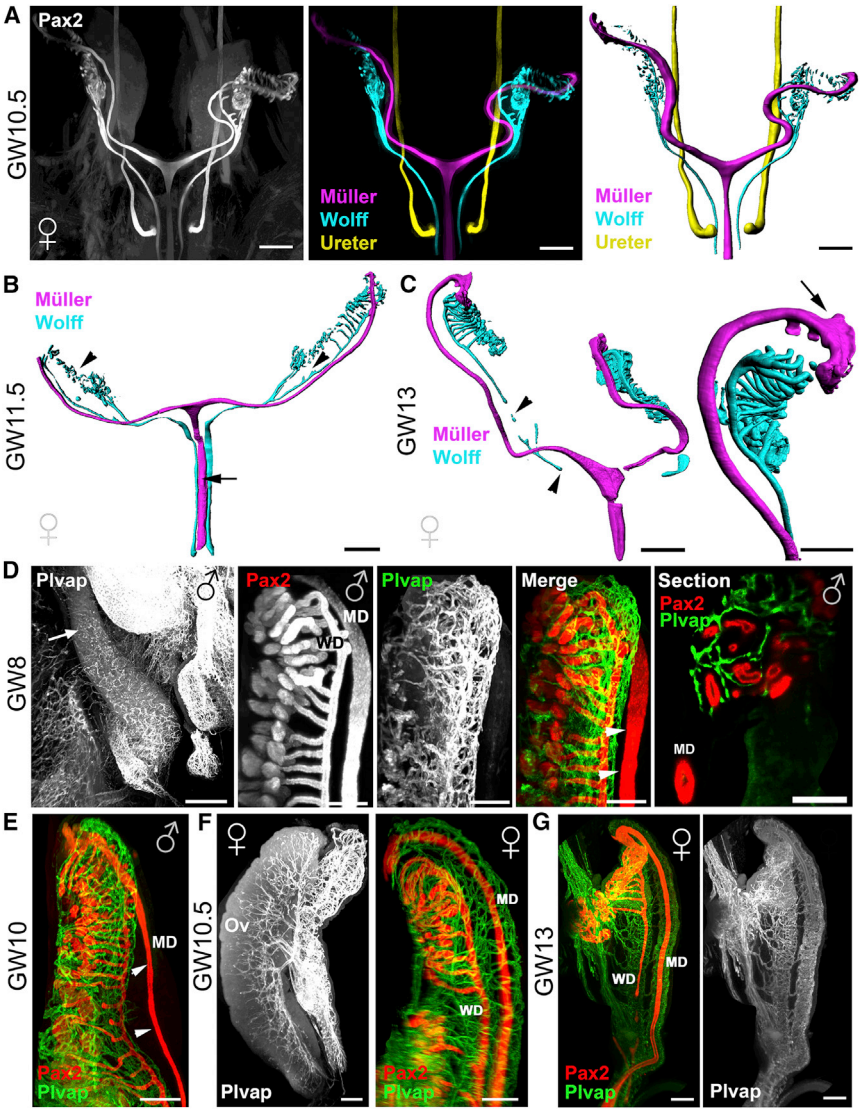

Figure 7. Comparative 3D Analysis of the Urogenital System Development in Female and Male Embryos

All panels are LSFM images of solvent-cleared embryos and fetuses.

(A) Original LSFM image (left), segmented/colorized (middle) and 3D (right) images of the urogenital system in a GW10.5 female fetus labeled with Pax2. The Wolffian ducts (cyan) are continuous and the Müllerian (magenta) ducts have fused.

(B) Genital system of a GW11.5 female fetus stained with Pax2 after segmentation and 3D rendering. The arrow indicates the developing uterus and upper vagina. The Wolffian ducts start to regress (arrowheads).

(C) Genital system of a GW13 female fetus stained with Pax2 after segmentation and 3D rendering. The size of the future uterus has increased and the Wolffian ducts have significantly regressed (arrowheads). The right panel is a high magnification at the level of the apical part of the Müllerian duct showing the developing fimbriae of the oviduct (arrow).

(D and E) Vasculature of the developing gonads.

(D) GW8 testis labeled for Pax2 and Plvap. A dense Plvap+ capillary network covers all the testis (arrow on the left) and the Wolffian duct (WD). By contrast, the Müllerian duct (MD) is not vascularized (arrowheads). The right panel is an optical section (1.2 μm) through the right testis and MD.

(E) At GW10, the MD is still devoid of capillaries in male. (F, G) GW10.5 and GW13 ovaries labeled for Pax2 and Plvap. A dense vascular network covers the ovary (Ov). Unlike in males, both the Müllerian and Wolffian ducts are densely vascularized. Abbreviations: ♀, female; ♂, male; MD, Müllerian ducts; WD, Wolffian ducts; OV, ovary.

Scale bars, 500 μm in (A), (B), and (C, left panel), 270 μm in (C, right panel), 100 μm in (D, middle and right panels), 160 μm in (D, left panel), 200 μm in (E)–(G).

See also Figure S5 and Figure S6.

Non-invasive medical imaging of embryos and fetuses in utero has made remarkable progress. This includes 3D and 4D obstetrical ultrasonography that can generate holographic images of the embryo (Baken et al., 2015; Pooh et al., 2011) but mostly provides information about surface features and cavities, as well as 3D power Doppler, which visualizes the embryo vasculature (Weisstanner et al., 2015). In addition, in utero magnetic resonance imaging provides a good appreciation of the developing CNS in the fetus (Weisstanner et al., 2015) and diffusion tensor imaging (DTI) tractography is now used as a prenatal diagnostic of callosal dysgenesis as early as GW20 (Jakab et al., 2015). While these techniques represent valuable tools to visualize the gross anatomy of the fetus, they lack in resolution and are insufficient to resolve the molecular signature of individual cells or to know their organization within organs. Recently, whole-organ histology and 3D-reconstruction analysis based on the digital alignment of embryo sections has been performed (de Bakker et al., 2016), but it is extremely time consuming. Our method, which preserves the 3D organization of the organs while achieving a great cellular resolution, is rapid, highly reproducible, and should provide clinicians with a reliable spatial framework for the correlation of in utero and postmortem 3D images of embryos and fetuses.

The simplicity of this method, its robustness (for example, we could label endothelial cells in a fresh frozen GW5 embryo kept for 11 years at −80°C, unpublished data), and its sensitivity will facilitate its transfer to human embryology laboratories. Its use for the analysis of embryos and fetuses with genetic diseases and malformations will improve our understanding of their etiology.

Currently, the main limitations of our method are the availability of human embryos, the number of antibody combinations (a maximum of four at this time), the compatibility of the antibodies with our protocol (Table S1) and the storage of large size light-sheet image datasets. Nevertheless, the spectrum of future investigations and applications of this method in the field of embryology and fetology are countless. For instance, defining how many cells give rise to an individual organ and understanding how cell

numbers are regulated during development is essential to understanding the process of organogenesis. Here, we show that whole-mount immunostaining with transcription factors and proliferation markers (KI67 and H3P) expressed in specific cell types (such as stem cells and muscle precursors) can be efficiently carried out in cleared embryos and fetal organs. This opens the possibility to obtain the number of cells expressing these factors, as well as map their localization in the body and estimate the rate of cell proliferation during the first trimester of human gestation—a critical period for various diseases in which tissue growth is perturbed. The recent surge of Zika virus infection and reports of its deleterious effects in the brain (Oliveira Melo et al., 2016) has demonstrated how incomplete our understanding of human embryo development is and how little we know about the mechanisms through which pathogens, toxins, and mutations impact embryogenesis. Our work shows that it should be possible in the near future to build a reference 3D atlas of the developing human. As a first step in this direction, all our 3D datasets are made available on a dedicated website (https://transparent-human-embryo.com/) that will also serve as a repository for additional embryology 3D data generated from our laboratory and others. This reference 3D atlas of the developing human and specific organs and systems not only represents a powerful educational online tool for researchers, educators, and students worldwide, but will allow 3D printing of anatomical models for didactic purposes in health sciences education programs.

STAR★METHODS

Detailed methods are provided in the online version of this paper and include the following:

- KEY RESOURCES TABLE
- CONTACT FOR REAGENT AND RESOURCE SHARING
- EXPERIMENTAL MODEL AND SUBJECT DETAILS
- METHOD DETAILS
  - Tissue Collection and Processing
  - Sex determination
  - Bleaching
  - Whole-Mount Immunostaining
  - Agarose Embedding
  - Tissue Clearing
  - Methanol clearing
  - 3D Imaging and Image Processing
  - Image Processing
- DATA AND SOFTWARE AVAILABILITY
- ADDITIONAL RESOURCES

SUPPLEMENTAL INFORMATION

Supplemental Information includes seven figures, one table, and seven movies and can be found with this article online at http://dx.doi.org/10.1016/j.cell.2017.03.008.

An audio PaperClip is available at http://dx.doi.org/10.1016/j.cell.2017.03.008#mmc9.

AUTHOR CONTRIBUTIONS

S.A.M., P.G., and F.C. collected, staged, and fixed the embryos and fetuses. M.B. and S.A.M. did the clearing and immunostaining. M.B. and D.G. performed the LSFM acquisitions and Imaris data processing. A.C. and M.B. did the figures. A.C., M.B., D.G., and G.C. analyzed the data. A.C. and P.G. wrote the manuscript. All authors corrected the manuscript.

ACKNOWLEDGMENTS

We thank the midwives of the Gynaecology Department, Jeanne de Flandres Hospital of Lille (Centre d'Orthogénie), France, for their assistance and support. We also thank Robin Vigouroux, Reha Erzurumlu, and Peter Kozulin for correcting the manuscript, Yorick Gitton and Stéphane Fouquet (Institut de la Vision, Imaging Facility) for their help with the database, and Olivier Pourquié, Domna Karagogeos, William Stallcup, Carmen Birchmeier, and Jean-François Brunet for kindly providing some antibodies. Myog and Pax7 antibodies were obtained from the Developmental Studies Hybridoma Bank. We are also grateful to Olivier Pourquié, José Sahel, Constantino Sotelo, and Nicole Le Douarin for helpful discussions. This work was supported by the Institut National de la Santé et de la Recherche Médicale (INSERM), France (grant number U1172), Agence Nationale de la Recherche (ANR), France (ANR-14-CE12-0015-01 to P.G., ANR-14-CE13-0004-01 to A.C.). It was performed in the frame of the LABEX LIFESENSES (reference ANR-10-LABX-65) supported by French state funds managed by the ANR within the Investissements d'Avenir programme under reference ANR-11-IDEX-0004-02.

Received: November 18, 2016
Revised: February 23, 2017
Accepted: March 3, 2017
Published: March 23, 2017

REFERENCES

Abe, S., Rhee, S.K., Osonoi, M., Nakamura, T., Cho, B.H., Murakami, G., and Ide, Y. (2010). Expression of intermediate filaments at muscle insertions in human fetuses. J. Anat. *217*, 167–173.

Aven, L., and Ai, X. (2013). Mechanisms of respiratory innervation during embryonic development. Organogenesis *9*, 194–198.

Baken, L., van Gruting, I.M.A., Steegers, E.A.P., van der Spek, P.J., Exalto, N., and Koning, A.H.J. (2015). Design and validation of a 3D virtual reality desktop system for sonographic length and volume measurements in early pregnancy evaluation. J. Clin. Ultrasound *43*, 164–170.

Bastide, P., Darido, C., Pannequin, J., Kist, R., Robine, S., Marty-Double, C., Bibeau, F., Scherer, G., Joubert, D., Hollande, F., et al. (2007). Sox9 regulates cell proliferation and is required for Paneth cell differentiation in the intestinal epithelium. J. Cell Biol. *178*, 635–648.

Belle, M., Godefroy, D., Dominici, C., Heitz-Marchaland, C., Zelina, P., Hellal, F., Bradke, F., and Chédotal, A. (2014). A simple method for 3D analysis of immunolabeled axonal tracts in a transparent nervous system. Cell Rep. *9*, 1191–1201.

Betters, E., Liu, Y., Kjaeldgaard, A., Sundström, E., and Garcia-Castro, M.I. (2010). Analysis of early human neural crest development. Dev. Biol. *344*, 578–592.

Blechschmidt, E. (1977). The Beginnings of Human Life (New York, NY: Springer New York).

Bondurand, N., and Sham, M.H. (2013). The role of SOX10 during enteric nervous system development. Dev. Biol. *382*, 330–343.

Bondurand, N., Kobetz, A., Pingault, V., Lemort, N., Encha-Razavi, F., Couly, G., Goerich, D.E., Wegner, M., Abitbol, M., and Goossens, M. (1998). Expression of the SOX10 gene during human development. FEBS Lett. *432*, 168–172.

Bourgeois, F., Messéant, J., Kordeli, E., Petit, J.M., Delers, P., Bahi-Buisson, N., Bernard, V., Sigoillot, S.M., Gitiaux, C., Stouffer, M., et al. (2015). A critical and previously unsuspected role for doublecortin at the neuromuscular junction in mouse and human. Neuromuscul. Disord. *25*, 461–473.

Breiteneder-Geleff, S., Soleiman, A., Kowalski, H., Horvat, R., Amann, G., Kriehuber, E., Diem, K., Weninger, W., Tschachler, E., Alitalo, K., and Kerjaschki, D. (1999). Angiosarcomas express mixed endothelial phenotypes of blood and

lymphatic capillaries: podoplanin as a specific marker for lymphatic endothelium. Am. J. Pathol. *154*, 385–394.

Brennan, J., Karl, J., and Capel, B. (2002). Divergent vascular mechanisms downstream of Sry establish the arterial system in the XY gonad. Dev. Biol. *244*, 418–428.

Bryson-Richardson, R.J., and Currie, P.D. (2008). The genetics of vertebrate myogenesis. Nat. Rev. Genet. *9*, 632–646.

Casoni, F., Malone, S.A., Belle, M., Luzzati, F., Collier, F., Allet, C., Hrabovszky, E., Rasika, S., Prevot, V., Chédotal, A., et al. (2016). Development of the neurons controlling fertility in humans: New insights from 3D imaging and transparent fetal brains. Dev. *143*.

Chung, A.S., and Ferrara, N. (2011). Developmental and pathological angiogenesis. Annu. Rev. Cell Dev. Biol. *27*, 563–584.

Coveney, D., Cool, J., Oliver, T., and Capel, B. (2008). Four-dimensional analysis of vascularization during primary development of an organ, the gonad. Proc. Natl. Acad. Sci. USA *105*, 7212–7217.

de Bakker, B.S., de Jong, K.H., Hagoort, J., de Bree, K., Besselink, C.T., de Kanter, F.E.C., Veldhuis, T., Bais, B., Schildmeijer, R., Ruijter, J.M., et al. (2016). An interactive three-dimensional digital atlas and quantitative database of human development. Science *354*, aag0053.

De la Cuadra-Blanco, C., Peces-Peña, M.D., Carvallo-de Moraes, L.O., Herrera-Lara, M.E., and Mérida-Velasco, J.R. (2013). Development of the platysma muscle and the superficial musculoaponeurotic system (human specimens at 8-17 weeks of development). ScientificWorldJournal *2013*, 716962.

des Portes, V., Francis, F., Pinard, J.M., Desguerre, I., Moutard, M.L., Snoeck, I., Meiners, L.C., Capron, F., Cusmai, R., Ricci, S., et al. (1998). doublecortin is the major gene causing X-linked subcortical laminar heterotopia (SCLH). Hum. Mol. Genet. *7*, 1063–1070.

Dodt, H.U., Leischner, U., Schierloh, A., Jährling, N., Mauch, C.P., Deininger, K., Deussing, J.M., Eder, M., Zieglgänsberger, W., and Becker, K. (2007). Ultramicroscopy: three-dimensional visualization of neuronal networks in the whole mouse brain. Nat. Methods *4*, 331–336.

Elima, K., Henttinen, T., Irjala, H., Salmi, M., and Health, N.P. (2005). Molecular identification of PAL-E, a widely used endothelial cell marker. Hematology *106*, 1–24.

Ertürk, A., Mauch, C.P., Hellal, F., Förstner, F., Keck, T., Becker, K., Jährling, N., Steffens, H., Richter, M., Hübener, M., et al. (2011). Three-dimensional imaging of the unsectioned adult spinal cord to assess axon regeneration and glial responses after injury. Nat. Med. *18*, 166–171.

Espinosa-Medina, I., Outin, E., Picard, C.A., Chettouh, Z., Dymecki, S., Consalez, G.G., Coppola, E., and Brunet, J.F. (2014). Neurodevelopment. Parasympathetic ganglia derive from Schwann cell precursors. Science *345*, 87–90.

Fritsch, H., Richter, E., and Adam, N. (2012). Molecular characteristics and alterations during early development of the human vagina. J. Anat. *220*, 363–371.

Fujimoto, T. (2001). Nishimura's collection of human embryos and related publications. Congenit. Anom. (Kyoto) *41*, 67–71.

Galambos, C., and deMello, D.E. (2007). Molecular mechanisms of pulmonary vascular development. Pediatr. Dev. Pathol. *10*, 1–17.

Gasser, R.F. (1967). The development of the facial muscles in man. Am. J. Anat. *120*, 357–375.

Georgas, K.M., Armstrong, J., Keast, J.R., Larkins, C.E., McHugh, K.M., Southard-Smith, E.M., Cohn, M.J., Batourina, E., Dan, H., Schneider, K., et al. (2015). An illustrated anatomical ontology of the developing mouse lower urogenital tract. Development *142*, 1893–1908.

Gilbert, P.W. (1957). The Origin and Development of the Human Extrinsic Ocular Muscles. Contrib. Embryol. *36*, 59–78.

Gleeson, J.G., Allen, K.M., Fox, J.W., Lamperti, E.D., Berkovic, S., Scheffer, I., Cooper, E.C., Dobyns, W.B., Minnerath, S.R., Ross, M.E., and Walsh, C.A. (1998). Doublecortin, a brain-specific gene mutated in human X-linked lissencephaly and double cortex syndrome, encodes a putative signaling protein. Cell *92*, 63–72.

Hanley, N.A., Hagan, D.M., Clement-Jones, M., Ball, S.G., Strachan, T., Salas-Cortés, L., McElreavey, K., Lindsay, S., Robson, S., Bullen, P., et al. (2000). SRY, SOX9, and DAX1 expression patterns during human sex determination and gonadal development. Mech. Dev. *91*, 403–407.

Hashimoto, R. (2003). Development of the human Müllerian duct in the sexually undifferentiated stage. Anat. Rec. A Discov. Mol. Cell. Evol. Biol. *272*, 514–519.

Hassan, B.A., and Hiesinger, P.R. (2015). Beyond Molecular Codes: Simple Rules to Wire Complex Brains. Cell *163*, 285–291.

Heanue, T.A., and Pachnis, V. (2007). Enteric nervous system development and Hirschsprung's disease: advances in genetic and stem cell studies. Nat. Rev. Neurosci. *8*, 466–479.

Hersch, M., and Ganchrow, D. (1980). Scanning electron microscopy of developing papillae on the tongue of human embryos and fetuses. Chem. Senses *5*, 331–341.

His, W. (1881). Anatomie menschlicher Embryonen (Leipzig: Vogel).

Jacob, M., Yusuf, F., and Jacob, H.J. (2012). Development, Differentiation and Derivatives of the Wolffian and Müllerian Ducts. In The Human Embryo, S. Yamada, ed. (InTech), pp. 143–166.

Jakab, A., Kasprian, G., Schwartz, E., Gruber, G.M., Mitter, C., Prayer, D., Schöpf, V., and Langs, G. (2015). Disrupted developmental organization of the structural connectome in fetuses with corpus callosum agenesis. Neuroimage *111*, 277–288.

Kanahashi, T., Yamada, S., Tanaka, M., Hirose, A., Uwabe, C., Kose, K., Yoneyama, A., Takeda, T., and Takakuwa, T. (2016). A Novel Strategy to Reveal the Latent Abnormalities in Human Embryonic Stages from a Large Embryo Collection. Anat. Rec. (Hoboken) *299*, 8–24.

Karagogeos, D., Pourquié, C., Kyriakopoulou, K., Tavian, M., Stallcup, W., Péault, B., and Pourquié, O. (1997). Expression of the cell adhesion proteins BEN/SC1/DM-GRASP and TAG-1 defines early steps of axonogenesis in the human spinal cord. J. Comp. Neurol. *379*, 415–427.

Keibel, F., and Elze, C. (1908). Normentafeln zur Entwicklungsgeschichte der Wirbeltiere. Achtes Heft. Des Menschen (Jena: Verlag von Gustav Fischer).

Keibel, F., and Mall, F.P. (1910). Manual of human embryology, *Volume 1* (Philadelphia, London: Lippincott).

King, D.F., and King, L.A. (1986). A brief historical note on staining by hematoxylin and eosin. Am. J. Dermatopathol. *8*, 168.

Little, M.H., Brennan, J., Georgas, K., Davies, J.A., Davidson, D.R., Baldock, R.A., Beverdam, A., Bertram, J.F., Capel, B., Chiu, H.S., et al. (2007). A high-resolution anatomical ontology of the developing murine genitourinary tract. Gene Expr. Patterns *7*, 680–699.

Locher, H., Frijns, J.H.M., van Iperen, L., de Groot, J.C.M.J., Huisman, M.A., and Chuva de Sousa Lopes, S.M. (2013). Neurosensory development and cell fate determination in the human cochlea. Neural Dev. *8*, 20.

Ludwig, K.S., and Landmann, L. (2005). Early development of the human mesonephros. Anat. Embryol. (Berl.) *209*, 439–447.

Maeda, Y., Davé, V., and Whitsett, J.A. (2007). Transcriptional control of lung morphogenesis. Physiol. Rev. *87*, 219–244.

Mall, F.P. (1905). On the development of the blood-vessels of the brain in the human embryo. Am. J. Anat. *4*, 1–18.

Metzger, R.J., Klein, O.D., Martin, G.R., and Krasnow, M.A. (2008). The branching programme of mouse lung development. Nature *453*, 745–750.

Morgan, L.M. (2009). Icons of Life: A Cultural History of Human Embryos (Berkeley: University of California Press).

Nakayama, A., Miura, H., Ooki, M., and Harada, S. (2015). During development intense Sox2 expression marks not only Prox1-expressing taste bud cell but also perigemmal cell lineages. Cell Tissue Res. *359*, 743–753.

Norman, J.R. (1923). Methods and technique of reconstruction. J. R. Microsc. Soc. *43*, 37–56.

O'Brien, L.L., Guo, Q., Lee, Y., Tran, T., Benazet, J.-D., Whitney, P.H., Valouev, A., and McMahon, A.P. (2016). Differential regulation of mouse and human nephron progenitors by the Six family of transcriptional regulators. Development *143*, 595–608.

O'Rahilly, R. (1983). The timing and sequence of events in the development of the human reproductive system during the embryonic period proper. Anat. Embryol. (Berl.) *166*, 247–261.

O'Rahilly, R., and Müller, F. (1987). Developmental stages in human embryos. Carnegie Inst. Washingt. Publ., 637.

Okubo, T., Pevny, L.H., and Hogan, B.L.M. (2006). Sox2 is required for development of taste bud sensory cells. Genes Dev. *20*, 2654–2659.

Oliveira Melo, A.S., Malinger, G., Ximenes, R., Szejnfeld, P.O., Alves Sampaio, S., and Bispo de Filippis, A.M. (2016). Zika virus intrauterine infection causes fetal brain abnormality and microcephaly: tip of the iceberg? Ultrasound Obstet. Gynecol. *47*, 6–7.

Orvis, G.D., and Behringer, R.R. (2007). Cellular mechanisms of Müllerian duct formation in the mouse. Dev. Biol. *306*, 493–504.

Pan, C., Cai, R., Quacquarelli, F.P., Ghasemigharagoz, A., Lourbopoulos, A., Matryba, P., Plesnila, N., Dichgans, M., Hellal, F., and Ertürk, A. (2016). Shrinkage-mediated imaging of entire organs and organisms using uDISCO. Nat. Methods. *13*, 859–867.

Parera, M.C., van Dooren, M., van Kempen, M., de Krijger, R., Grosveld, F., Tibboel, D., and Rottier, R. (2005). Distal angiogenesis: a new concept for lung vascular morphogenesis. Am. J. Physiol. Lung Cell. Mol. Physiol. *288*, L141–L149.

Parysek, L.M., Chisholm, R.L., Ley, C.A., and Goldman, R.D. (1988). A type III intermediate filament gene is expressed in mature neurons. Neuron *1*, 395–401.

Pooh, R.K., Shiota, K., and Kurjak, A. (2011). Imaging of the human embryo with magnetic resonance imaging microscopy and high-resolution transvaginal 3-dimensional sonography: human embryology in the 21st century. Am. J. Obstet. Gynecol. *204*, 77.e1–77.e16.

Renier, N., Wu, Z., Simon, D.J., Yang, J., Ariel, P., and Tessier-Lavigne, M. (2014). iDISCO: a simple, rapid method to immunolabel large tissue samples for volume imaging. Cell *159*, 896–910.

Renier, N., Adams, E.L., Kirst, C., Wu, Z., Azevedo, R., Kohl, J., Autry, A.E., Kadiri, L., Umadevi Venkataraju, K., Zhou, Y., et al. (2016). Mapping of Brain Activity by Automated Volume Analysis of Immediate Early Genes. Cell *165*, 1789–1802.

Richardson, D.S., and Lichtman, J.W. (2015). Clarifying Tissue Clearing. Cell *162*, 246–257.

Rockich, B.E., Hrycaj, S.M., Shih, H.P., Nagy, M.S., Ferguson, M.A.H., Kopp, J.L., Sander, M., Wellik, D.M., and Spence, J.R. (2013). Sox9 plays multiple roles in the lung epithelium during branching morphogenesis. Proc. Natl. Acad. Sci. USA *110*, E4456–E4464.

Sabin, F.R. (1909). The lymphatic system in human embryos, with a consideration of the morphology of the system as a whole. Am. J. Anat. *9*, 43–91.

Sarkar, A., and Hochedlinger, K. (2013). The sox family of transcription factors: versatile regulators of stem and progenitor cell fate. Cell Stem Cell *12*, 15–30.

Schuster, C., Mildner, M., Botta, A., Nemec, L., Rogojanu, R., Beer, L., Fiala, C., Eppel, W., Bauer, W., Petzelbauer, P., and Elbe-Bürger, A. (2015). Development of Blood and Lymphatic Endothelial Cells in Embryonic and Fetal Human Skin. Am. J. Pathol. *185*, 2563–2574.

Sparrow, M.P., Weichselbaum, M., and McCray, P.B. (1999). Development of the innervation and airway smooth muscle in human fetal lung. Am. J. Respir. Cell Mol. Biol. *20*, 550–560.

Tellier, A.L., Amiel, J., Delezoide, A.L., Audollent, S., Augé, J., Esnault, D., Encha-Razavi, F., Munnich, A., Lyonnet, S., Vekemans, M., and Attié-Bitach, T. (2000). Expression of the PAX2 gene in human embryos and exclusion in the CHARGE syndrome. Am. J. Med. Genet. *93*, 85–88.

Unver Dogan, N., Uysal, I.I., Karabulut, A.K., Seker, M., and Ziylan, T. (2010). Communications between the palmar digital branches of the median and ulnar nerves: A study in human fetuses and a review of the literature. Clin. Anat. *23*, 234–241.

Weisstanner, C., Kasprian, G., Gruber, G.M., Brugger, P.C., and Prayer, D. (2015). MRI of the Fetal Brain. Clin. Neuroradiol. *25*(*Suppl 2*), 189–196.

Yamada, S., Samtani, R.R., Lee, E.S., Lockett, E., Uwabe, C., Shiota, K., Anderson, S.A., and Lo, C.W. (2010). Developmental atlas of the early first trimester human embryo. Dev. Dyn. *239*, 1585–1595.

Yang, Y., and Oliver, G. (2014). Development of the mammalian lymphatic vasculature. J. Clin. Invest. *124*, 888–897.

Zawiliński, J., Litwin, J.A., Nowogrodzka-Zagórska, M., Gorczyca, J., and Miodoński, A.J. (2001). Vascular system of the human spinal cord in the prenatal period: a dye injection and corrosion casting study. Ann. Anat. *183*, 331–340.

STAR★METHODS

KEY RESOURCES TABLE

REAGENT or RESOURCE	SOURCE	IDENTIFIER
Antibodies		
Rabbit polyclonal anti-Barhl1	Sigma-Aldrich	Cat# HPA004809; RRID: AB_1078266
Mouse monoclonal anti-ALCAM/BEN (Clone F84.1)	Santa Cruz Biotechnology	Cat# sc 53980; RRID:AB_831079
Goat polyclonal anti-Choline Acetyltransferase	Millipore	Cat# AB144P; RRID:AB_2079751
Rabbit polyclonal anti-mouse collagen Type IV	MD Biosciences	Cat# MD20451; RRID:AB_10576569
Rat monoclonal anti-Ctip2	Abcam	Cat# ab18465; RRID:AB_2064130
Mouse monoclonal anti-D2-40 Endothelial marker	BioLegend	Cat# 916601; RRID:AB_2565182
Goat anti-Doublecortin (C18)	Santa Cruz Biotechnology	Cat# sc-8066; RRID:AB_2088494
Rabbit monoclonal anti-Doublecortin	Cell Signaling Technology	Cat# 4604S; RRID:AB_10693771
Mouse monoclonal anti-Foxp1 (Clone JC12)	Abcam	Cat# ab32010; RRID:AB_1141518
Goat polyclonal anti-Foxp2 (N16)	Santa Cruz Biotechnology	Cat# sc-21069; RRID:AB_2107124
Rabbit polyclonal anti-Foxp2	Abcam	Cat# ab16046; RRID:AB_2107107
Rabbit polyclonal anti-Phospho-Histone H3(Ser10)	Cell Signaling Technology	Cat# 9701S; RRID:AB_331534
Rabbit polyclonal anti-Islet1	Abcam	Cat# ab20670; RRID:AB_881306
Rabbit polyclonal anti-Ki67	Abcam	Cat# ab15580; RRID:AB_443209
Guinea-pig monoclonal anti-Lmx1b	Carmen Birchmeier, MaxDelbrück Center for Molecular Medicine;Berlin, Germany	Cat# Lmx1b; RRID:AB_2314752
Rabbit polyclonal anti-Gonadotropin releasing hormone	R. Benoit, McGill University; Montreal; Canada	Cat# LR5; RRID:AB_2314605
Mouse monoclonal anti-Myosin Heavy Chain (Clone A4.1025)	Millipore	Cat# 05-716; RRID:AB_309930
Mouse monoclonal anti-Myosin, Skeletal, Fast	Sigma-Aldrich	Cat# M4276; RRID:AB_477190
Mouse monoclonal anti-Myogenin	DSHB	Cat# F5D AB_2146602
Mouse monoclonal anti-Myosin (Smooth)	Sigma-Aldrich	Cat# M7786; RRID:AB_477239
Rabbit monoclonal anti-Olig-2	Millipore	Cat# AB9610 RRID:AB_10141047
Mouse monoclonal anti-Parvalbumine	Swant	Cat# 235 RRID:AB_10000343
Goat polyclonal anti-Human Pax2	R and D Systems	Cat# AF3364; RRID:AB_10889828
Rabbit polyclonal anti-Pax6	Millipore	Cat# AB5409; RRID:AB_2315065
Mouse Anti-Chicken PAX7 Monoclonal Antibody, Unconjugated	DSHB	Cat# pax7 RRID:AB_528428
Mouse monoclonal anti-Peripherin (Clone 8G2)	Millipore	Cat# MAB1527; RRID:AB_2284441
Rabbit polyclonal anti-Peripherin	Millipore	Cat# AB1530; RRID:AB_90725
Rabbit polyclonal anti-Phox2b	J.-F. Brunet, Ecole Normale Superieure; Paris; France	Cat# Phox2b RRID:AB_2315160
Mouse monoclonal anti-PLVAP (Clone 174/2)	Abcam	Cat# ab81719; RRID:AB_1658370
Rabbit polyclonal anti-PROX1	Acris Antibodies GmBH	Cat# DP3501P; RRID:AB_1006742
Goat polyclonal anti-Human ROBO3	R and D Systems	Cat# AF3076; RRID:AB_2181865
Mouse monoclonal anti-SATB2 (Clone SATBA4B10)	Abcam	Cat# ab51502; RRID:AB_882455
Rabbit polyclonal anti-SIX2	Proteintech Group	Cat# 11562-1-AP; RRID:AB_2189084
Mouse monoclonal anti-Actin, alpha-Smooth Muscle	Sigma-Aldrich	Cat# A2547; RRID:AB_476701
Goat polyclonal anti-Sox10 (N-20)	Santa Cruz Biotechnology	Cat# sc-17342; RRID:AB_2195374
Rabbit polyclonal anti-SOX2	Abcam	Cat# ab97959; RRID:AB_2341193

(*Continued on next page*)

Continued

REAGENT or RESOURCE	SOURCE	IDENTIFIER
Goat polyclonal anti-Sox2 (Y-17)	Santa Cruz Biotechnology	Cat# sc-17320; RRID:AB_2286684
Rabbit polyclonal anti-Sox9	Millipore	Cat# AB5535; RRID:AB_2239761
Goat polyclonal anti-Contactin-2/TAG-1	R and D Systems	Cat# AF4439; RRID:AB_2044647
Rabbit polyclonal anti-Contactin-2/TAG-1	Domna Karagogeos, University of Crete, Heraklion, Crete, Greece	DOI:10.1523/JNEUROSCI.2574-10.2010
Rabbit polyclonal anti-TBR1	Abcam	Cat# ab31940; RRID:AB_2200219
Rabbit polyclonal anti-Tlx3	Carmen Birchmeier, MaxDelbrück Center for Molecular Medicine;Berlin, Germany	Cat# Tlx3; RRID:AB_2532145
Mouse monoclonal anti-Neuronal Class III beta-Tubulin	Covance Research Products	Cat# MMS-435P; RRID:AB_2313773
Rabbit polyclonal anti-Tyrosine Hydroxylase	Millipore	Cat# AB152; RRID:AB_390204
Donkey Anti-Chicken IgG (H+L) Alexa Fluor 488 AffiniPure	Jackson ImmunoResearch Labs	Cat# 703-545-155; RRID:AB_2340375
Goat anti-Chicken IgY (H+L) Alexa Fluor 488 conjugate	Thermo Fischer Scientific	Cat# A-11039; RRID:AB_2534096
Alexa Fluor® 594 AffiniPure Donkey Anti-Guinea Pig IgG (H+L)	Jackson ImmunoResearch Labs	Cat# 706-585-148 RRID:AB_2340474
Donkey Anti-Guinea Pig IgG (H+L) Cy3 AffiniPure (min x Bov,Ck,Gt,Hms,Hrs,Hu,Ms,Rb,Rat,Shp,Sr Prot)	Jackson ImmunoResearch Labs	Cat# 706-165-148; RRID:AB_2340460
Donkey Anti-Guinea Pig IgG (H+L) Alexa Fluor 488 AffiniPure	Jackson ImmunoResearch Labs	Cat# 706-545-148; RRID:AB_2340472
Donkey Anti-Rabbit IgG (H+L) Alexa Fluor 488 AffiniPure	Jackson ImmunoResearch Labs	Cat# 711-545-152; RRID:AB_2313584
Donkey Anti-Rabbit IgG (H+L) Alexa Fluor 647 AffiniPure	Jackson ImmunoResearch Labs	Cat# 711-605-152; RRID:AB_2492288
Donkey Anti-Rabbit IgG H&L (Alexa Fluor 488) preadsorbed antibody	Abcam	Cat# ab150061; RRID:AB_2571722
Donkey Anti-Rabbit IgG (H+L) Cy3 AffiniPure (min X Bov,Ck,Gt,GP,Sy Hms,Hrs,Hu,Ms,Rat,Shp Sr Prot)	Jackson ImmunoResearch Labs	Cat# 711-165-152; RRID:AB_2307443
Donkey Anti-Rat IgG (H+L) Cy3 AffiniPure (min x Bov,Ck,Gt,Sy Hms,Hrs,Hu,Ms,Rb, Shp,Sr Prot)	Jackson ImmunoResearch Labs	Cat# 712-165-153; RRID:AB_2340667
Donkey Anti-Rat IgG (H+L) Alexa Fluor 647 AffiniPure	Jackson ImmunoResearch Labs	Cat# 712-605-153; RRID:AB_2340694
Bovine Anti-Goat IgG (H+L) Alexa Fluor 488 AffiniPure	Jackson ImmunoResearch Labs	Cat# 805-545-180; RRID:AB_2340883
Bovine Anti-Goat IgG (H+L) Alexa Fluor 647 AffiniPure	Jackson ImmunoResearch Labs	Cat# 805-605-180; RRID:AB_2340885
Bovine Anti-Goat IgG (H+L) Cy3 AffiniPure (min x Bov, Ck,Gt,Sy Hms,Hrs,Hu,Ms,Rb, Rat Sr Prot)	Jackson ImmunoResearch Labs	Cat# 805-165-180; RRID:AB_2340880
Donkey Anti-Goat IgG H&L (Alexa Fluor 647) preadsorbed	Abcam	Cat# ab150135; RRID: N/A
Donkey Anti-Goat IgG (H+L) Cy3 AffiniPure	Jackson ImmunoResearch Labs	Cat# 705-165-147; RRID:AB_2307351
Donkey Anti-Mouse IgG (H+L) Cy3 AffiniPure	Jackson ImmunoResearch Labs	Cat# 715-165-150 RRID:AB_2340813
Donkey Anti-mouse IgG H&L (Alexa Fluor 555) preadsorbed	Abcam	Cat# ab150106; RRID: N/A
Donkey anti-Mouse IgG (H+L) Secondary Antibody, Alexa Fluor 488	Molecular Probes	Cat# A-21202 RRID:AB_141607
Goat anti-Mouse IgM Heavy Chain Secondary Antibody, Alexa Fluor 488	Molecular Probes	Cat# A-21042; RRID:AB_141357
Donkey Anti-Mouse IgG (H+L) Alexa Fluor 647 AffiniPure	Jackson ImmunoResearch Labs	Cat# 715-605-150; RRID:AB_2340862

(*Continued on next page*)

Continued

REAGENT or RESOURCE	SOURCE	IDENTIFIER
Donkey anti-Mouse IgG Secondary Antibody, Alexa Fluor 568	Termo Fisher Scientific	Cat# A10037; RRID:AB_2534013
Tested, non-working antibodies	Table S1	
Biological Samples		
Human tissue	This paper	N/A
Chemicals, Peptides, and Recombinant Proteins		
Tetrahydrofuran Anhydre > 99.9% (THF)	Sigma-Adrich	Cat# 186562 CAS Number 109-99-9
Dichloromethane (DCM)	Sigma-Adrich	Cat# 270997 CAS Number: 75-09-2
Dibenzyl ether (DBE)	Sigma-Adrich	Cat# 108014 CAS Number: 103-50-4
Methanol (MeOH)	VWR Chemicals	Cat# 20847.360 CAS Number: 67-56-1
Hydrogen peroxide solution (H_2O_2)	Sigma-Adrich	Cat# 216763 CAS Number: 7722-84-1
Agarose	Carl ROTH	Cat# 2267.4 CAS Number: 9012-36-6
Gelatin	VWR Chemicals	Cat# 24350.262 CAS Number: 9000-70-8
Thimerosal	Sigma-Adrich	Cat# T8784-5g CAS Number: 54-64-8
Triton X-100	Sigma-Adrich	Cat# X100-500ml CAS Number: 9002-93-1
SYLGARD 184 SILICONE ELASTOMER KIT	DOW CORNING	Cat# SYLGARD 184 SILICONE ELASTOMER KIT CAS Number: N/A
Deposited Data		
Raw and analyzed data	This paper	https://transparent-human-embryo.com/
Sequence-Based Reagents		
SRY sense 5′-AGCGATGATTACAGTCCAGC-3′	This paper	N/A
SRY antisense 5′-CCTACAGCTTTGTCCAGTGG-3′	This paper	N/A
FGF16 sense 5′- CGGGAGGGATACAGGACTAAAC-3′	This paper	N/A
FGF16 antisense 5′- CTGTAGGTAGCATCTGTGGC-3′	This paper	N/A
Software and Algorithms		
Imspector software	LaVision Biotec	http://www.lavisionbiotec.com/
Imaris x64 software (version 8.0.1)	Bitplane	http://www.bitplane.com/imaris/imaris; RRID:SCR_007370
ImageJ (1.50e, Java 1.8.0_60, 64-bit)	NIH	https://imagej.nih.gov/ij/; RRID:SCR_003070
iMovie (version 10.1.1)	Apple	http://www.apple.com/fr/imovie/

CONTACT FOR REAGENT AND RESOURCE SHARING

Further information and requests for resources and reagents should be directed to and will be fulfilled by the Lead Contact, Dr Alain Chédotal (alain.chedotal@inserm.fr).

All data have been deposited in https://transparent-human-embryo.com/ and access to the high-resolution movies and image stacks is regulated via an MTA agreement available online.

EXPERIMENTAL MODEL AND SUBJECT DETAILS

Human embryos (<GW8.5) and fetuses (≥GW8.5) were obtained with the parent's written informed consent (Gynaecology Hospital Jeanne de Flandres, Lille, France) with approval of the local ethic committee (protocol N° PFS16-002). Tissues were made available in accordance with the French bylaw (Good practice concerning the conservation, transformation and transportation of human tissue to be used therapeutically, published on December 29, 1998). Permission to utilize human tissues was obtained from the French agency for biomedical research (Agence de la Biomédecine, Saint-Denis La Plaine, France). For this study, we used 7 embryos at Carnegie Stage 17 (CS17) corresponding to 41 days of development (E46) or gestational week 6 (GW6) (n = 1) (O'Rahilly and Müller, 1987), CS19/E46/GW7 (n = 2), CS21/E51/GW7.5 (n = 1), CS23/E56/GW8 (n = 3), and 29 fetuses at GW8.5 (n = 2), GW9 (n = 3), GW9.5 (n = 5), GW10 (n = 6), GW10.5 (n = 2), GW11 (n = 3), GW11.5 (n = 1), GW12 (n = 1), GW13 (n = 1), GW13.5 (n = 1) and GW14 (n = 4). This included 9 females and 11 males (sex was undetermined for the others).

METHOD DETAILS

Tissue Collection and Processing

For embryos younger than 8 gestation weeks (GW), the developmental age was assessed using the Carnegie stages (CS) (O'Rahilly and Müller, 1987). Gestation weeks of each embryo or fetus studied were estimated based on the information about: 1) menstrual weeks, 2) morphology, 3) length (crown-rump), 4) craniofacial structures, and 5) position of the tongue. Embryos and fetuses, were fixed by immersion in 4% PFA at 4°C for 1 to 5 days depending on size. For fetuses between GW9-14, tissues were dissected after fixation and post-fixed in 4% PFA at 4°C overnight. Embryos and fetuses, did not present any malformations.

Sex determination

Sex determination was obtained by isolating DNA from extracted tissues using lysis buffer containing 0.1mg/ml proteinase K, 5M Sodium Chloride, 20% Sodium dodecyl sulfate, 1M Tris, pH 8.0 solution in water and stored at 54°C overnight. DNA was precipitated with isopropanol (1:1) and re-suspended in RNase/DNase-free water for 3 hr at 65°C. A PCR was performed in a thermocycler (Bio-rad) using the following steps: 94°C for 3 min and 35 cycles of 94°C for 1 min; 56°C for 30 s; 72°C for 30 s and 72°C for 5 min. For genotyping the following primers were used: SRY sense 5′-AGCGATGATTACAGTCCAGC-3′ and antisense 5′-CCTACAGCTTTGTC CAGTGG-3′; FGF16 sense 5′- CGGGAGGGATACAGGACTAAAC-3′ and antisense 5′- CTGTAGGTAGCATCTGTGGC-3′. Only 20 embryos could be assessed, as prior tissue processing prevented DNA extraction for other cases.

Bleaching

To remove pigmentation and reduce signal-to-noise ratio related to hematomas, the tissue bleaching was carried out (Renier et al., 2014). The samples were dehydrated for 1hr at RT in ascending concentrations of methanol in 1XPBS (50%, 80%, 100%). The samples were then treated overnight at 4°C with a 6% hydrogen peroxide solution in 100% methanol. The following day, samples were re-hydrated for 1hr at RT in descending concentrations of methanol (100% twice, 80%, 50%) and washed in 1XPBS during 1hr. Samples were kept at 4°C for further processing.

Whole-Mount Immunostaining

Samples were permeabilized and blocked by rotation at 70 rpm in 1XPBS containing 0.2% gelatin (Prolabo), and 0.5% Triton X-100 (Sigma-Aldrich) (PBSGT) at RT (Belle et al., 2014). For immunostaining, samples were transferred to a solution containing 0.1% saponin (10μg/mL) in PBSGT together with the primary antibodies (listed in the Key Resource Table and in Table S1) and placed at 37°C (Benchmark, Incu-Shaker Mini), with rotation at 70 rpm, for 7 to 14 days depending on tissue size and density. This was followed by six washes of 30 min in PBSGT at RT. Next, secondary antibodies (listed in the Key Resource Table) were diluted in a solution containing 0.1% saponin (10μg/mL) in PBSGT and passed through a 0.22 μm filter. Samples were incubated at 37°C (Benchmark, Incu-Shaker Mini) in the secondary antibody solution overnight or for 2 days depending on sample size and density. After six washes of 30 min in PBSGT at RT, samples were stored in the dark at 4°C in until tissue clearing. The protocol was similar for single and multiple labeling.

Agarose Embedding

As previously described (Belle et al., 2014; Renier et al., 2014) small samples were embedded in agarose prior to clearing and processing with the LSFM. To embed samples, 1.5% agarose (Roth) was prepared in TAE 1X (Invitrogen).

Tissue Clearing

3DISCO

For all tissue clearing, a modified 3DISCO clearing protocol was used. All incubation steps were performed in dark conditions at RT in a fume hood, on a tube rotator (SB3, Stuart) at 14 rpm, using a 15 mL centrifuge tube (TPP, Dutscher). Samples were first dehydrated in ascending concentrations (50%, 80%, and 100%) of tetrahydrofuran (THF; anhydrous, containing 250 ppm butylated hydroxytoluene inhibitor, Sigma-Aldrich) diluted in H_2O. The initial 50% THF bath was done overnight while the 80% and 100% THF incubations were left for 1.5 hr each. Samples next underwent a delipidation step of 30 min in dichloromethane (DCM; Sigma-Aldrich) followed by an overnight clearing step in dibenzyl ether (DBE; Sigma-Aldrich). The next day, samples were stored in individual light-absorbing glass vials (Rotilabo, Roth) at RT. In these conditions, samples could be stored and imaged for up to 9 months without any significant fluorescence loss.

Methanol clearing

For large tissues, methanol clearing was used to achieve higher transparency using a modification from the iDISCO+ protocol (Renier et al., 2016). Whole embryos ($\leq$GW8) and tissues (> GW8) were dehydrated in methanol/1XPBS series (n = 7): 20%, 40%, 60%, 80%, 100% x2 for 1 hr each at RT on a tube rotator (SB3, Stuart) at 14 rpm, using a 15 mL centrifuge tube (TPP, Dutscher) covered with aluminum foil to avoid contact with light. Then samples were incubate overnight in 2/3 DCM/ 1/3 Methanol. After 30 min in 100% DCM, samples were transferred to DBE.

3D Imaging and Image Processing

3D imaging was performed as previously described. Acquisitions were performed by using an ultramicroscope I (LaVision BioTec) with the ImspectorPro software (LaVision BioTec). The light sheet was generated by a laser (wavelength 488, 561 or 640nm, Coherent Sapphire Laser, LaVision BioTec) and focused using two cylindrical lenses. Two adjustable protective lenses were applied for small and large working distances. A binocular stereomicroscope (MXV10, Olympus) with a 2x objective (MVPLAPO, Olympus) was used at different magnifications (0.63x, 0.8x, 1x, 1.25x, 1.6×, 2x, 2.5x, 3.2x, 4x, 5x, and 6.3x). The corresponding zoom factors and numerical apertures are available at http://lavisionbiotec.com/ultramicroscope-ii-specifications.html.

Samples were placed in an imaging reservoir made of 100% quartz (LaVision BioTec) filled with DBE and illuminated from the side by the laser light. A PCO Edge SCMOS CCD camera (2,560 × 2,160 pixel size, LaVision BioTec) was used to acquire images. The step size between each image was fixed at 1 and 2 μm. All tiff images are generated in 16-bit. For large samples, a platform was created using PDMS (Sylgard) fixed to a sample holder from LaVision.

Image Processing

Images, 3D volume, and movies were generated using Imaris x64 software (version 8.0.1, Bitplane). Stack images were first converted to imaris file (.ims) using ImarisFileConverter and 3D reconstruction was performed using the ''volume rendering'' function. To facilitate image processing, images were converted to an 8-bit format. To obtain opaque visualizations, the normal shading view was applied. Optical slices were obtained using the ''orthoslicer'' tool. To isolate a specific region of the tissue, the surface tool was used and the mask option was selected. For isolation of smaller structures, i.e., nerve segmentation, the surface tool was manually applied and each nerve was subsequently pseudo-colored. For the hand, the foot, and the urogenital system, nerves and organs were initially segmented manually and visualized in 3D using the 3D rendering tool. In order to visualize bone structures in 3D, skin is artificially removed by segmentation and the contrast is modified using normal shading view. 3D pictures and movies were generated using the ''snapshot'' and ''animation'' tools. Movie reconstruction with .tiff series are done with ImageJ (1.50e, Java 1.8.0_60, 64-bit), titles and transitions addition have been done with iMovie (version 10.1.1).

DATA AND SOFTWARE AVAILABILITY

All movies and files are available through a dedicated website, https://transparent-human-embryo.com/.

ADDITIONAL RESOURCES

Access to the 3D image datasets is available through http://transparent-human-embryo.com/. The database was created with the help of keen eye technologies.

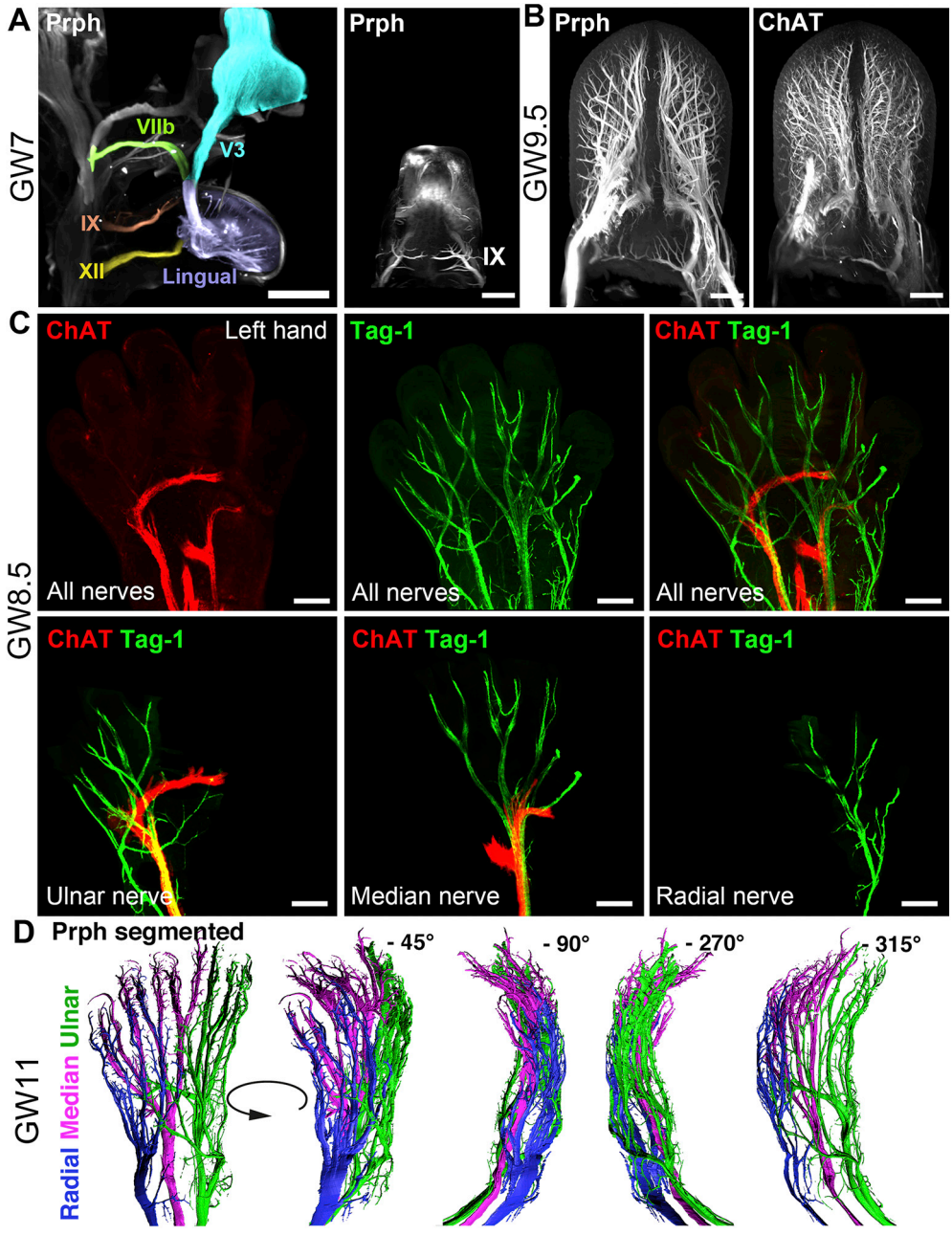

Figure S1. Peripheral Innervation of the Tongue and Hand of 3DISCO-Cleared Embryos, Related to Figure 1

All panels are images acquired by light sheet fluorescence microscopy (LSFM) of 3DISCO-cleared embryos and fetuses.

(A) GW7 embryo stained for Prph. The left panel is a segmentation of the four nerves innervating the tongue (right side). The trigeminal nerve (V3, mandibular subdivision) and the chorda tympani of the facial nerve (VIIb or Wrisberg nerve) contribute to the lingual nerve. The two other nerves are the glossopharyngian (IX) and hypoglossus (XII). The right panel is a ventral view of the tongue.

(B) Dorsal views of the tongue in a GW9.5 fetus labeled for Prph (left) and ChAT (right).

(C) Dorsal view of the left hand at GW8.5 labeled for Tag-1 (sensory nerves) and ChAT (motor nerves). All nerves (ulnar, median, and radial) are shown on the upper panels. The lower panels represent the ulnar, the median, and the radial nerves of the hand individually. The ulnar and the median nerves are comprised of both sensory and motor axons.

(D) LSFM images of a GW11 right hand labeled for Prph after segmentation and pseudocolorization. The median (magenta), radial (blue), and ulnar (green) nerves are shown together. From left to right, images correspond to a counterclockwise rotation of an angle indicated on the panels from the dorsal view position on the left.

Scale bars, 500 μm in A (left panel), 300 μm in A (right panel) and B, 200 μm in C.

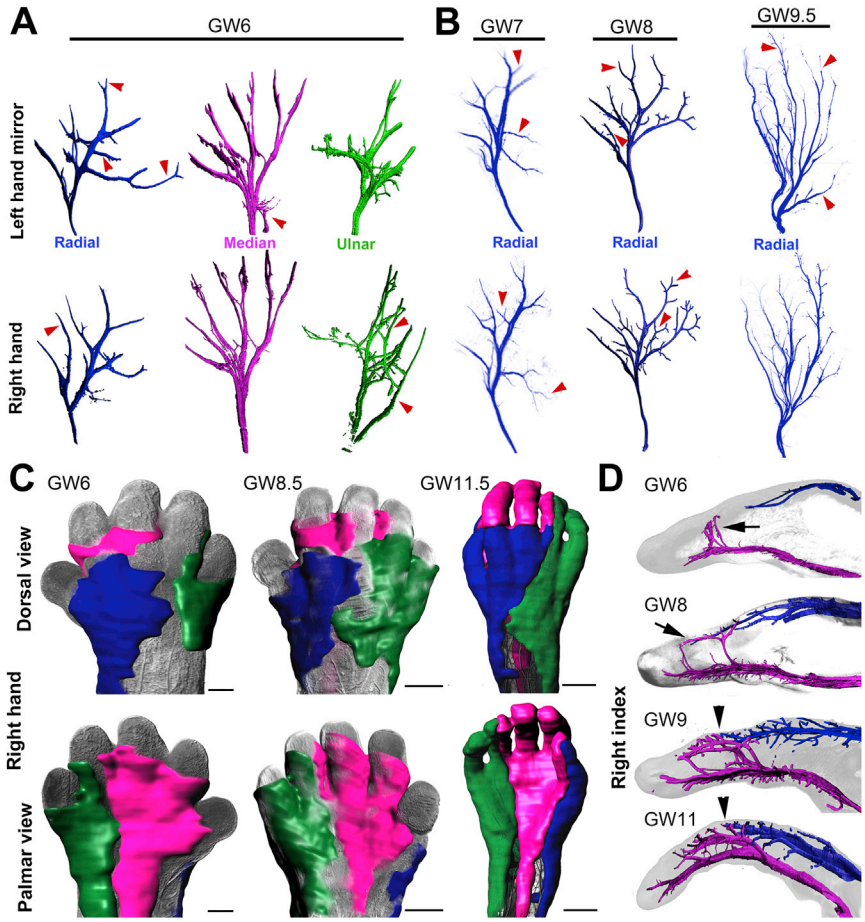

Figure S2. Development of Sensory Nerve Branches in the Human Hand, Related to Figure 2

(A and B) LSFM images after segmentation and 3D rendering of the innervation of GW6–GW9.5 embryos (dorsal views). The upper panels are mirror images of left hand nerves and the lower panels show right hands from the same individuals. Red arrowheads indicate branches found uniquely in one of the hands.

(A) At GW6, the median nerve branches (magenta) are very similar in both the right and the left hand whereas the radial (blue) and ulnar (green) nerves have distinct branching patterns between the left/right hands.

(B) Radial nerves at GW7, GW8, and GW9.5. Some branches are only found in either the left or right hands.

(C) Dorsal and palmar 3D views of GW6, GW8.5, and GW11.5 right hands in which the surface of the skin overlaying the radial (blue), ulnar (green), and median (magenta) nerves have been pseudo-colored.

(D) Side views illustrating the development of the innervation of the medial (magenta) and radial (blue) nerves in the right index finger at GW6, GW8, GW9, and GW11. Short arrows indicate the dorsal branches of the median nerve that extend ahead of the radial nerve and arrowheads the border between, the radial and medial nerves.

Scale bars, 200 μm in C (left), 300 μm in C (middle), and 1,000 μm in C (right).

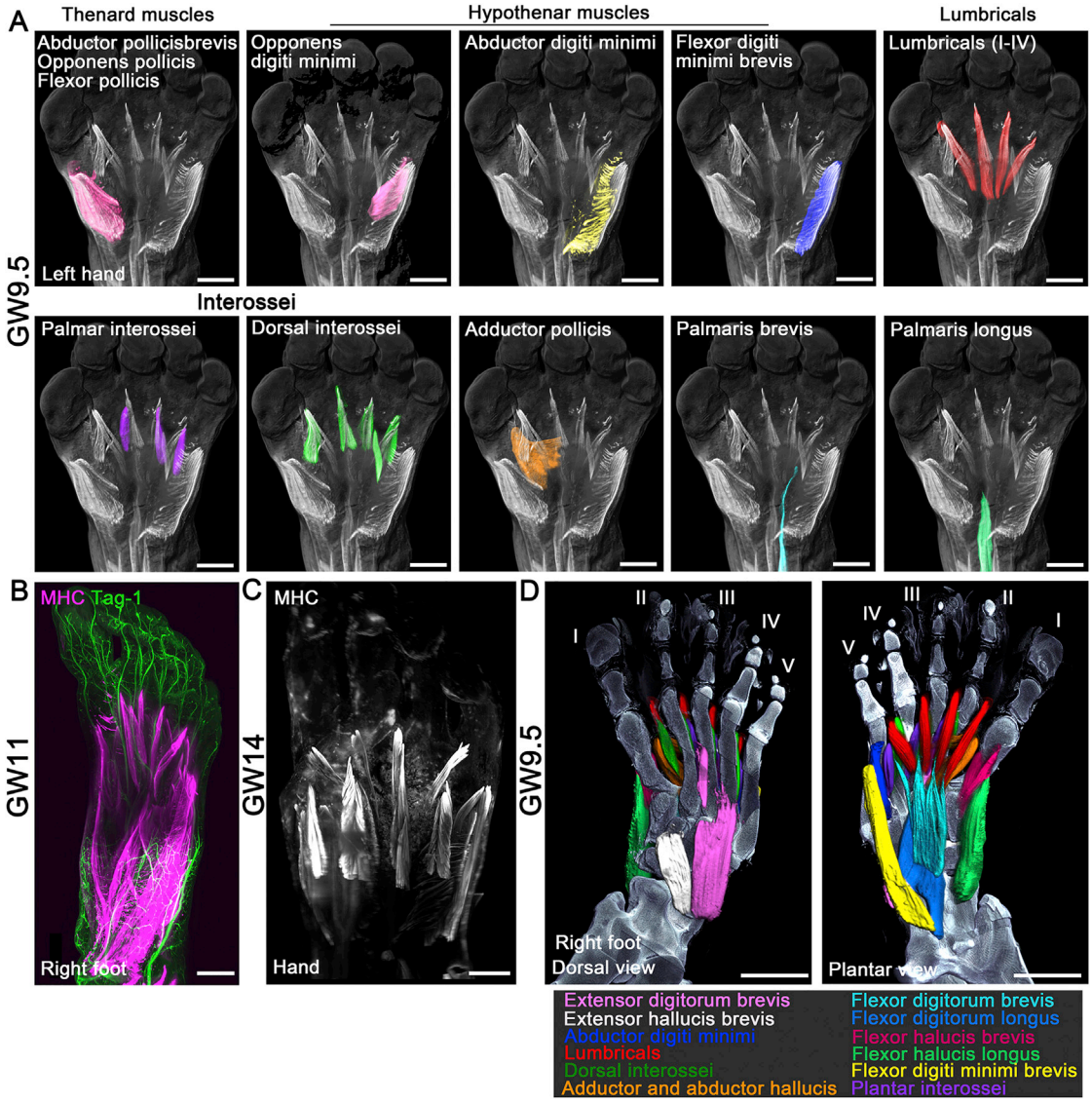

Figure S3. Segmentation of the Musculature in Human Embryos, Related to Figure 3

All panels are LSFM images of 3DISCO-cleared embryos and fetuses.

(A) Palmar view of the left hand in a GW9.5 fetus labeled for MHC. Each panel shows the segmentation of individual muscles or group of muscles.

(B) Dorsal view of the right foot of a GW11 fetus labeled with antibodies against MHC and Tag-1. Muscles (magenta) and sensory nerves (green) can be seen.

(C) Dorsal view of the muscles of the right hand of a GW14 embryo labeled for MHC.

(D) Dorsal and plantar views of the right foot of a GW9.5 fetus labeled for MHC. All muscles have been individually segmented, pseudo-colored and bones contours were extracted from LSFM images.

Abbreviations: I–V, toes. Scale bars, 400 μm in A,B, 1000 μm in C, 500 μm in D.

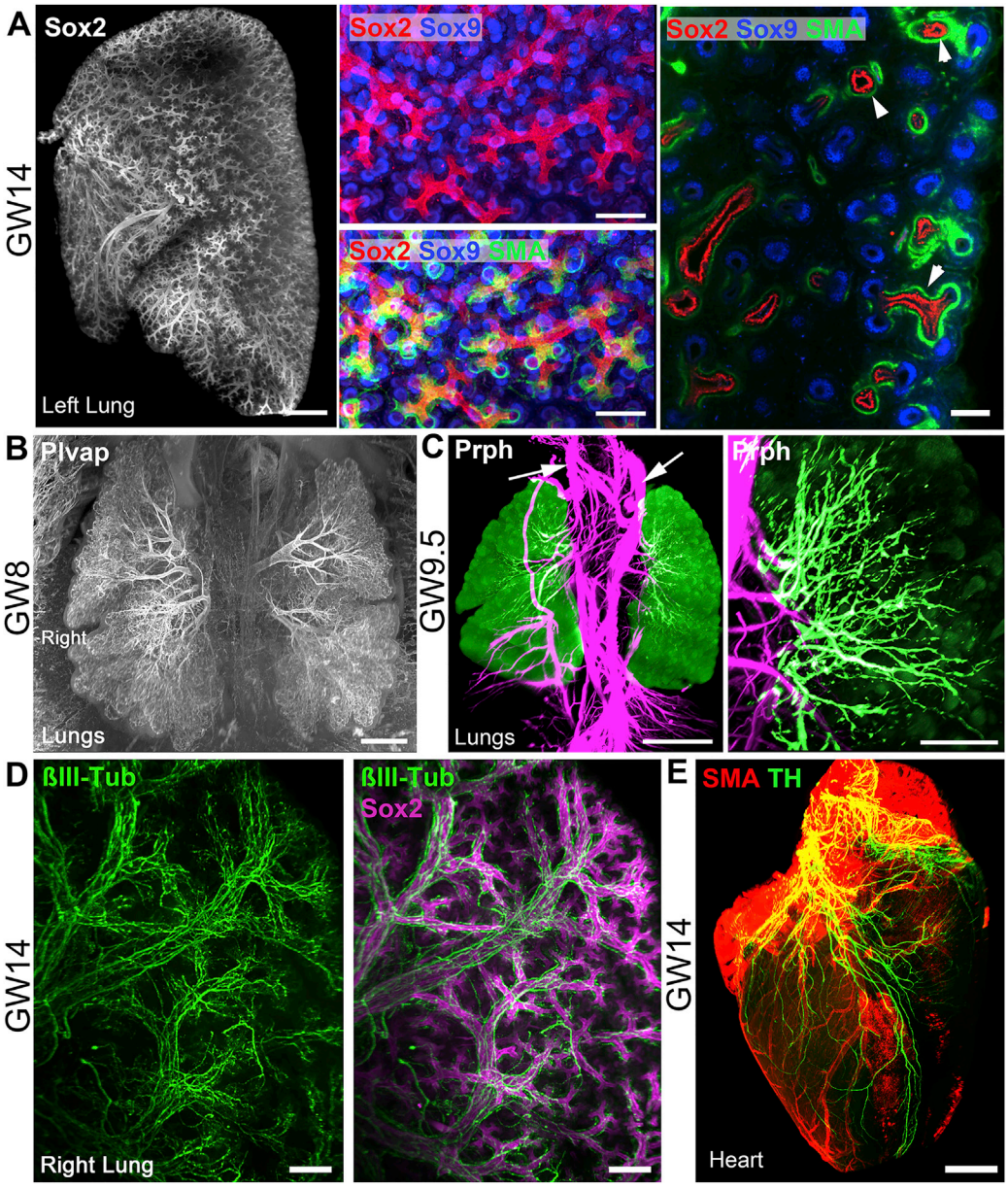

Figure S4. Development of the Cardiopulmonary System in Human Embryos, Related to Figure 5

All panels are LSFM images of solvent-cleared embryos and fetuses.

(A) Left lung from a GW14 fetus immunostained for Sox2, Sox9 and SMA. Sox2 is expressed along the airway tubules except in the distal buds which only express Sox9. SMA+ smooth muscles ensheathe the Sox2+ epithelium (arrowheads) but not the Sox9+ buds. The right panel is an optical section (3 μm z projection).

(B) Vasculature of the lungs from a GW8 embryo labeled for Plvap.

(C) Innervation of the lungs from a GW9.5 fetus labeled with anti-Prph. The vagus nerves (arrows) send branches along the lung airways. The lungs and their innervation have been segmented and pseudo-colored in green.

(D) Innervation of the airway branches in a GW14 fetus, visualized with immuno-histochemistry with anti-ßIII tubulin and anti-Sox2. ßIII-tubulin+ axons extend along the Sox2+ epithelial tubules to the level of the distal epithelial buds (not labeled with Sox2).

(E) Dopaminergic (TH) innervation of the heart of a GW14 fetus. The large vessels are labeled with anti-SMA (see also Figure 6K).

Scale bars, 1,000 μm in A and C (left panels), 200 μm in A (middle panels), 100 μm in A (right panel), 400 μm in B, 300 μm in C (right panel) and D, 1,200 μm in E.

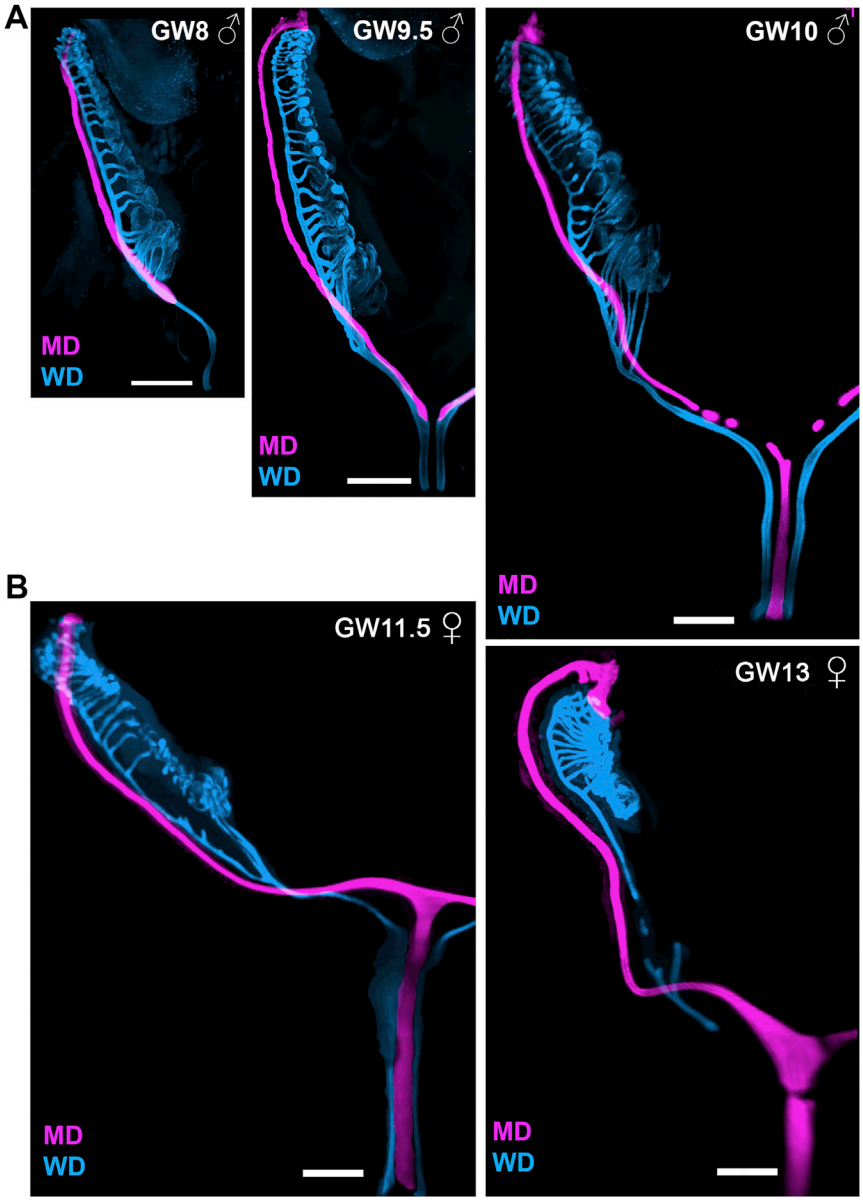

Figure S5. Development of the Müllerian and Wolffian Ducts in Male and Female Human Embryos, Related to Figure 6 and Figure 7

All panels are LSFM images of the genital tracts of solvent-cleared embryos and fetuses labeled with Pax2 antibody, segmented and pseudocolored. All images are at the same magnification.

(A) In males the Müllerian duct (MD) extends ventrally along the Wolffian duct (WD) and fuses with the opposite MD around GW9.5. The MDs then degenerate except the fused domain that will become the prostatic utricle.

(B) In females, the MDs fuse to form the uterus and vagina and the WDs regress.

Scale bars, 400 μm in A and B.

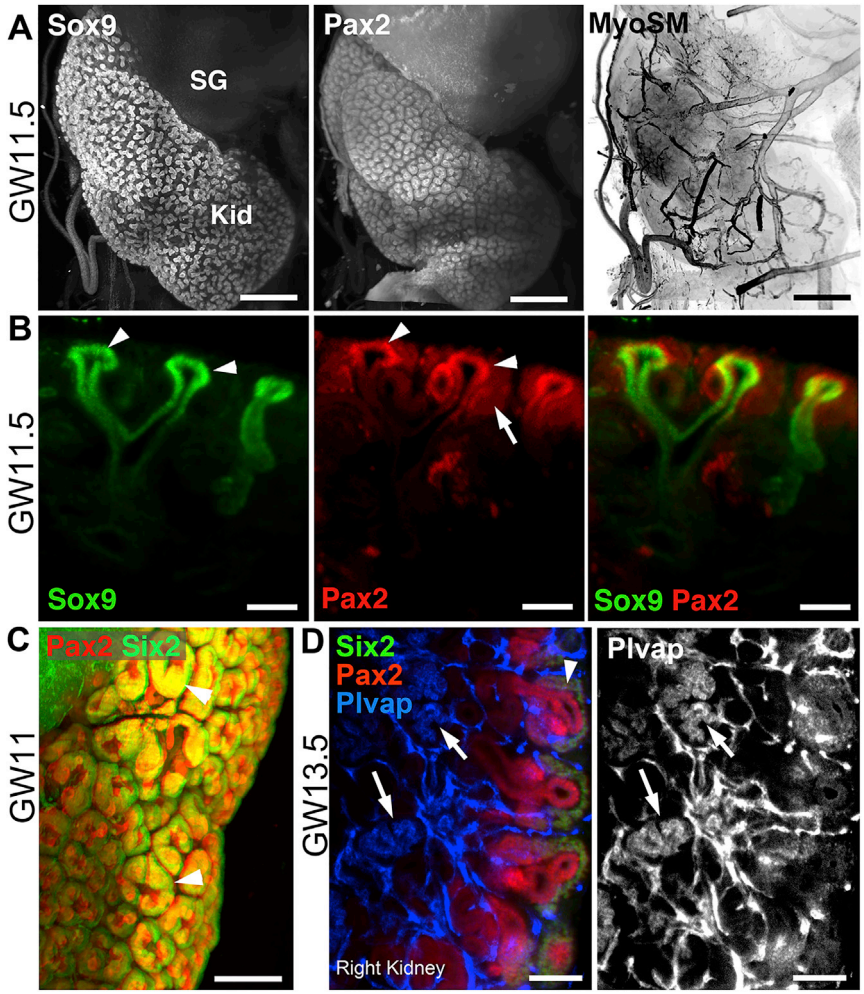

Figure S6. LSFM of the Developing Human Kidney, Related to Figure 7

All panels are LSFM images of 3DISCO-cleared fetuses.

(A and B) GW11.5 kidney labeled for Sox9, Pax2 and MyoSM. Sox9 and Pax2 are expressed in the developing kidney (Kid) but are absent from the suprarenal gland (SG). MyoSM labels arteries vascularizing the kidney.

(B) Is a single optical section (1 μm) through the cortex. Sox9 and Pax2 are expressed in the distal part of the ureteric buds (arrowheads). Pax2 is also expressed in the cap mesenchyme and developing nephrons (arrow).

(C) A GW11 kidney labeled for Pax2 and Six2. Both TFs are expressed in developing cap mesenchyme surrounding ureteric tips and renal vesicles (arrowheads).

(D) Single optical section (2 μm) through the kidney of a GW13.5 fetus labeled for Plvap, Six2, and Pax2. Six2 and Pax2 are co-expressed in the cap mesenchyme (arrowheads) but Pax2 is also expressed in tubules. Plvap staining shows the dense renal capillary network and glomeruli primordia (arrows).

Scale bars, 500 μm in A, 50 μm in B, 180 μm in C, and 70 μm in D.

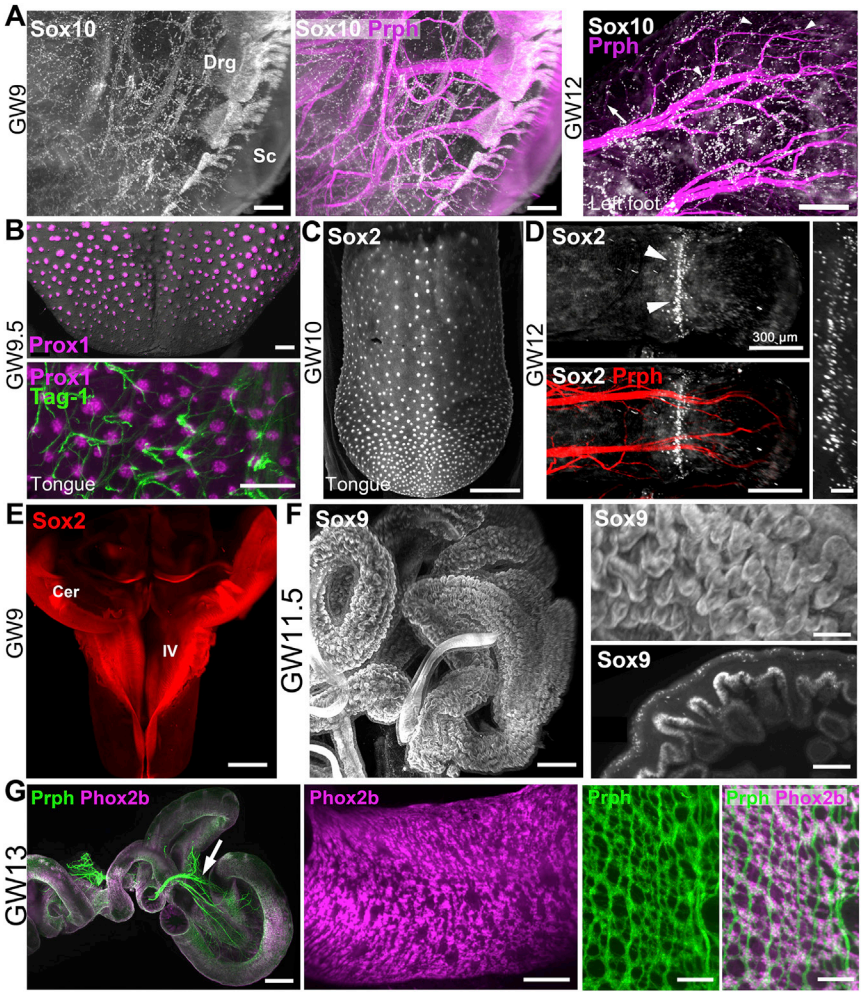

Figure S7. Transcription Factor Expression in Human Embryos, Related to Figure 5

All panels are LSFM images of solvent-cleared embryos and fetuses.

(A) GW9 and GW12 fetuses labeled for Sox10 and Prph. The left and middle panels illustrate Sox10+ cells at the level of the spinal cord (Sc) and dorsal root ganglia (Drg). The right panel shows Sox10 cells (including Schwann cell precursors) migrating along sensory nerves in the foot.

(B) Tongue of a GW9.5 fetus labeled for Prox1 and Tag-1. Prox1 is expressed by taste bud cell precursors and Tag-1 by sensory axons.

(C) Tongue of a GW10 fetus labeled with Sox2 antibodies. The pattern of developing Sox2+ taste buds is seen.

(D) Sox2 and Prph immunostaining of the index of a GW12 embryo. Sox2 is found in a narrow ring of cells (arrowheads) at the base of the presumptive finger nails (Prph stains sensory nerves). The right image is a higher magnification of the Sox2 cells.

(E) Sox2 staining of a GW9 hindbrain. Sox2 is highly expressed in progenitors of the ventricular zone lining the IVth ventricle (IV) and cerebellum (Cer).

(F) Sox9 immunostaining of the intestine of a GW11.5 embryo labeled for Sox9. Sox9 is highly expressed in the epithelium of the developing villi. The upper right panel is a high mag of intestinal villi. The bottom right panel is a 3.5 μm z projection.

(G) Whole-mount staining for Phox2b and Prph on a GW13 gut. The dense network of Phox2b immunoreactive enteric neurons is shown and their Prph+ connections. The vagus nerve innervating the gut is also seen (arrow).

Scale bars, 150 μm in A, 80 μm in B, 500 μm in C, E, F (left panel), 300 μm in D (left panels), 50 μm in D (right panel), 100 μm in F (right panels), 800 μm in G (left panel, 200 μm in G (middle panel), 70 μm in G (right panels).